A New Characterization Technique to Analyze Concentrator Photovoltaic Optical System Performance

by

Patrick Mcvey White

Thesis submitted to the Faculty of Graduate and Postdoctoral Studies in partial fulfillment
of the requirement for the Master of Applied Science
in Electrical and Computer Engineering

School of Electrical Engineering and Computer Science
University of Ottawa

***"If you can not explain it simply,
you don't understand it well enough."***

– Albert Einstein

Abstract

Concentrator photovoltaics is a promising renewable energy technology, especially for utility or large-scale deployments. Like all new technologies, it has obstacles and setbacks to overcome. More specifically, the optics in a concentrator photovoltaics system introduce non-uniform spatial and spectral illumination on the cell, which can change under different operating conditions. This work was put together to discover a new characterization technique capable of analyzing the performance of a concentrator photovoltaics and provide insight to the field on what is happening within the system, linking modeling results seen in the literature to these experimental outcomes. The thesis is composed of three journal papers written by the candidate, who's contributions are outlined at the beginning of each chapter.

In order to study the illumination profiles on the cells, a new method to characterize the optical components had to be developed. Previous version lacked the ability to control the temperature of the lens and had low spectral resolution of the irradiance profiles. To improve, a novel indoor measurement method was developed capable of spectrally imaging concentrator photovoltaics optics and recreate outdoor operating conditions in a controllable environment. With the calibrated system, our test-bench is capable of measuring the spectral distribution with a $10\mu\mathrm{m}^2$ resolution and characterizing the output of a system to within 3%. Exploiting this experimental technique, the individual effects of module misalignment, cell to primary distance, and lens temperature was studied for three leading technologies associated with the three generations of concentrator photovoltaics optical architectures.

Focusing on Fresnel-based concentrator optics, the performance of silicone on a glass module without a secondary optic is the most sensitive to operating conditions, where lens temperature can decrease the absolute efficiency resulting in a difference of 11% in the annual energy yield. The next two generations have secondary optics but are designed slightly differently. The truncated inverted pyramid, designed independently of the primary optic, favoured higher lens temperature values and there was only a difference of 1% in the energy yield calculation. The primary and secondary optics in the 4-fold Fresnel-Köhler are designed together, due to new development tools, and showed the highest stability under the different operating conditions, demonstrating that concentrator photovoltaics is on the right track to overcoming its onset issue. As the technology matures, future designs can improve on the issues characterized within this thesis.

Statement of Originality

The research presented in this dissertation was independently performed and analysed by the author under the supervision of Dr. Henry Schriemer and Dr. Karin Hinzer from September, 2014 to September, 2016. To the best of his knowledge, the results obtained and analysis contained in this MASc thesis are origional, unless otherwise noted.

Acknowledgement

To begin with, I would like to show my gratitude and thanks to Dr. Henry Schriemer and Dr. Karin Hinzer, who have both put in the time and effort to help me through my studies. Without Dr. Schriemer's suggestion and proposition during my last year as an undergrad, I would not have considered a Master's degree. Equally, Dr. Hinzer's enthusiasm and insight helped guide me through my graduate studies experience. Their handwork behind the scenes, always showing the utmost respect and trust towards their student, is a model that had made my graduate experience a memorable success. It was a privilege to be a part of the SUNLAB.

I am grateful to both Mark Yandt and Viktar Tatsiankou, both PhD students at the SUNLAB, for all of their patience, guidance, exemplary work ethic, and most importantly countless hours of troubleshooting issue with me. Extending this thanks to the senior members of the SUNLAB, Dr. Chris Valdivia, Dr. Joan Hayson, and Dr. John Cook, for their valuable inputs and editing while preparing for conferences and publication. This thanks extends to all members of the SUNLAB and associates; this group of intelligent individuals pushed my boundaries and made my experience a positive and exciting journey.

A very important thank you goes to the LCPV lab at CAE-INES in France where I completed my exchange over the summer of 2015. More specifically, thank you to Dr. Pierre Besson, it was a great experience working alongside him developing and collecting data to hammer out our first journal publication. The guidance of Dr. Mathiew Baudrit provided a great atmosphere where everyone worked hard to create a cohesive and driven group. Their generosity extended beyond the lab and provided me a true experience of life in France. I will never forget the group lunches, BBQs, and when Arnaud took me through *Les pics de Belledonne*, a true experience of the Alps' breathtaking views and exhilarating trails.

An honourable mention goes to my sister, Maegan White. Without her patience and ability to help decode my sentence structures, I don't know if people would be able to understand the content of my work. But seriously, both you and our mom, Lynne McVey, deserve a great thank you, your support and words of encouragement helped me complete this thesis!

List of Publications

This thesis work has led to the following publications:

(a) Journals

1. **Patrick McVey White**, Pierre Besson, Mathieu Baudrit, Henry Schriemer, and Karin Hinzer,"Influence of operating conditions on optical performance & annual energy yield for concentrator photovoltaics," advanced draft to be submitted to *Solar Energy*, October 2016.
2. P. Besson*, **P. McVey White***, C. Dominguez, P. Voarino, P. Garcia-Linares, M. Lemiti, H. Schriemer, K. Hinzer, and M. Baudrit, "Spectrally-resolved measurement of concentrated light distributions for Fresnel lens concentrators," Optics Express **24**, 397-407 (2016)

(c) International conference proceedings

3. **P. McVey White***, P. Besson, M. Baudrit, H. Schriemer, and K. Hinzer, "Effects of lens temperature on irradiance profile and chromatic aberration for CPV optics," *CPV-12*, Freiburg, Germany, AIP Conference Proceedings **1766**, 040004 (2016)
4. J. Haysom, **P. McVey White**, L. de la Salle, K. Hinzer, and H. Schriemer, "Multi-year ground-based irradiance dataset in a northern urban climate," *IEEE 43rd Photovoltaic Specialist Conference*, Portland, Oregon (2016)
5. J. P. D. Cook, P. Sharma, L. de la Salle, F. Carle, **P. McVey White**, V. Tatsiankou, J. E. Haysom, E. Dragomirescu, H. Schriemer, and K. Hinzer, "Refractive Concentrator Optics Architectures, Tracker Precision, and Cumulative Energy Harvest," *42nd IEEE Photovoltaic Specialists Conference*, New Orleans, United States, IEEE Conference Publications **1109**, 7356408 (2014)

(f) Other refereed contributions

6. **P. McVey White***, P. Sharma*, P. Besson, S. Fafard, M. Baudrit, S. Fafard, H. P. Schriemer, and K. Hinzer, "Effect of non-uniform illumination on triple junction solar cells under concentration," *CPV-11*, Bourget du lac, France (2015)
   (Poster presentation and published abstract)
7. **P. McVey White***, C. E. Valdivia, M. Yandt, S. Fafard, K. Hinzer, and H. P. Schriemer, "Multi-junction solar cell analysis with the tunable automated subcell characterization unit," *CPV-11*, Bourget du lac, France (2015)
   (Poster presentation and published abstract)

8. **P. McVey White**, A. H. Trojnar, M. Yandt, and K. Hinzer, "Multi-junction solar cell characterization instrument," *CMC Microsystems Texpo*, Gatineau, Quebec (2014)
   (Oral presentation and competition)
   Finalist for Brian L. Barge Award for Excellence in Microsystems Integration.
9. **P. McVey White***, M. Kelly*, N. Amyotte*, R. Li*, A. H. Trojnar, M. Yandt, and K. Hinzer, "Triple-Junction Solar Cell Characterization Instrument Using the Fill-Factor Bias Measurement Technique," Professional Engineers of Ontario Ottawa Chapter 2014 Student Papers Night (2014)
   (Oral presentation and 50 page technical report)
   Won Best Technical Report Content prize

(j) Non-refereed contributions

10. **P. McVey White** (2015) Optimization of Opto-Electrical Characterization of Concentrator Photovoltaic Modules. Technical report for Commissariat à l'énergie atomique et aux énergies alternatives (40 pages)
11. **P. McVey White** (2015) Calibration procedure to generate spectrum from multispectral images. Technical presentation for Commissariat à l'énergie atomique et aux énergies alternatives (55 pages)
12. **P. McVey White** (2015) Methodologies for characterizing Electrical, THermal, and Optical Devices (METHOD) hardware and software user manual. Operation manual for Commissariat à l'énergie atomique et aux énergies alternatives (50 pages)
13. **P. McVey White** and K. Hinzer (2015) A new analysys of the parameters of a flat panel PV energy yield calculation installed in Ottawa to generate the highest return of investment through maximizing the total amount of sunshine on the panel. Technical report for Sunlab research laboratory at the University of Ottawa (25 pages) *Link*
14. **P. McVey White**, S. Fafard, and K. Hinzer (2014) Tunable Automated Subcell Characterization (TASC) unit for the analysis of triple- and quadruple-junction solar cells. Invention disclosure filed to the University of Ottawa's Technology Transfer and Business Enterprise, November, 2014

Contents

List of acronyms and symbols

Acronyms

4FK	Four Fresnel-Köhler
ASTM	American Society for Testing and Materials
CAP	Acceptance angle product
CPV	Concentrator photovoltaic(s)
CSTC	Concentrator standard test conditions
DHI	Diffuse horizontal irradiance
DNI	Direct normal irradiance
GHI	Global horizontal irradiance
METHOD	Methodologies for characterizing electrical, thermal, and optical devices
MJSC	Multi-junction solar cell
NREL	National Renewable Energy Laboratory
PMMA	Polymethylmethacrylate
POE	Primary optical element
PV	Photovoltaic(s)
SMARTS	Simple model of the atmospheric radiative transfer of sunshine
SOE	Secondary optical element
SoG	Silicone on glass

Symbols

C	Calibration factor, unitless
C_g	Geometric concentration
F	Spectral irradiance in W/m^2/nm
FF	Fill factor
IV	Current-voltage
J_{sc}	Short circuit current density
η	Efficiency
P_{in}	Input power
S	Camera signal in counts
V_{oc}	Open circuit voltage

Chapter 1

Introduction

The demand for energy in today's society is rising as we strive to break barriers, continuously producing new developments. These efforts, while providing us with a higher standard of living, depend on an ample and steady supply of electricity. The Canadian residential energy demand, accountable for a mere 14% of the Canada's total demand, was 1,451 petajoules in 2015 and is projected to hit 1,730 petajoules by 2040 [B - 1]. To put this in perspective, the metro system in the heart of downtown Montreal requires only one petajoule for a full year of operation. Fossil fuels such as coal, oil, and natural gases have been shown as harmful to the environment and as being the root of many international disagreements, their resources are limited and depleting. On the other hand, renewable energies obtained from natural resources are capable of naturally replenishing themselves within a human lifespan. There are several key renewable energy possibilities including hydro, biofuel, wind, and solar, which begs the question: which renewable energy source will disrupt the industry? Solar power, commonly referred to as photovoltaic (PV), appears to be shining a light on the answer.

Simply put, PV uses a special type of material that converts sunlight, photons, into electricity, electrons. Semiconductor materials exhibit this photovoltaic effect and are the basis for the two current types of solar technologies: flat panel PV and concentrator PV (CPV). Silicone, a semiconductor material, has a large market share of the flat panel solar cell industry since it is relatively inexpensive and a well-understood material. However, silicone is limited by a fundamental conversion efficiency of around 25%. On the other hand, CPV uses a more expensive type of solar cells called multi-junction solar cells (MJSC), a stack of semiconductors with efficiency limits that exceed double of conventional silicon cells. The key to making CPV cost-competitive is the use of inexpensive concentrator optics to focus the sunlight, reducing the area of the solar cell and system costs. From 2010-2012, the cost of silicon cells fell drastically, reducing the confidence in CPV. So is it possible for CPV to be a competitor? To answer this question, let's see how it compares to other solar technologies.

Comparing different electricity-generating technologies is difficult, especially when the technologies have different market maturities. With a lower cumulative volume of global deployment, it is inevitable that the cost for a CPV system will be greater than PV. CPV systems have a higher cost of manufacturing and deployment along with more system components, all of which are commonly attributed to a young market that has yet to experience the benifits of an economy of scale, which motivates investment in research to drive manufacturing costs down and increase the efficiency of deployment. The relationship between deployment volume and system price, known as learning curve analysis, is regularly used to model pricing and comparison between energy systems. The learning rate provides an expected percentage drop in cost for every doubling of cumulative deployment volume. The learning curve analysis for the three dominant solar technologies was put together by Joan Haysom et al. [B - 2], which can be seen in figure 1.1. With a learning rate of 18%, this graph shows the potential for CPV over PV and concentrator solar power, which had a lower learning rate of 14 and 11%, respectively [B - 2]. Consequently, a stronger learning rate not only shows that the price for CPV is competative with PV but even has the potential to have the lowest price for the three solar technologies. If a cumulative deployment of 7,900 MW is reached by 2020, well within the annual growth rate seen by CPV, a $1/W is attenable [B - 2]. Over-

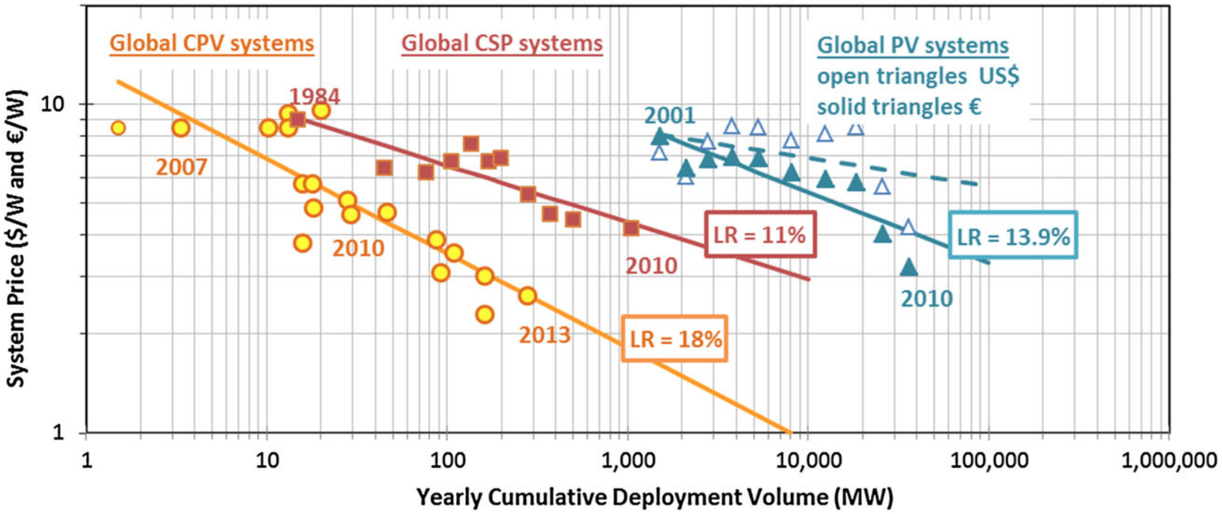

Figure 1.1: Learning curve plot, also know as log/log relationship system price, P, and cumulated deployment volume, V, for CPV, concentrator solar power, and PV Systerms[B - 2].

all, figure 1.1 provides a clear perspective on how the different solar technologies available today measure against each other. Looking forward, research and development and optics is increasing the efficiency of MJSC, making CPV technology the most promising option that will have a significant impact on the energy industry.

1.1 Overview of CPV systems

The concept behind CPV is relatable to anyone who has played with a magnifying glass. A lens can be used to create a small illumination area while retaining most of the incident power on the lens. Then, all that a CPV system does is place a highly efficient MJSC at this spot. This method not only reduces the area of semiconductor material, which is expensive, but improves the performance of the MJSC. Therefore, the two main components of a CPV system are a concentrator and MJSC, which can be seen in figure 1.2 where the light is being focused by a Fresnel lens at the top onto a packaged MJSC.

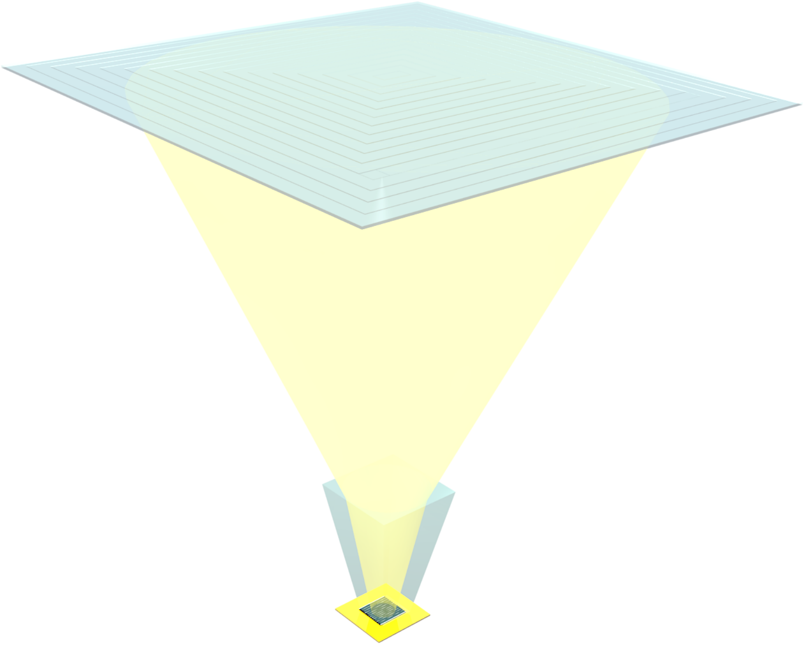

Figure 1.2: Visual representation of a concentrator photovoltaic system. The light exiting the primary optic, Fresnel lens at the top, enters the secondary optic uniformly illuminating the multi-junction solar cell, bottom.

Taking it one step forward, in order for a module to produce power under sunlight it will typically be made up of an optical train, a MJSC, thermal management, enclosure, and a tracking system. Each component can be different from module to module. First, the concentration of light can be achieved by either reflective or refractive optics. The majority of CPV systems use refraction with a Fresnel lens as the main optical element. Other companies, such as Morgan Solar, use waveguide technology for a thinner concept that has shown great potential in reducing manufacturing cost. An example of their system can be seen in figure 1.3. The MJSC and concentrators will be discussed in more detail in the next chapter.

Figure 1.3: Concentrator photovoltaic solar farm with Morgan Solar modules and dual-axis trackers [B - 3].

CPV has the potential to become a revolutionary technology and shows great performance in locations with high direct normal irradiance. The direct irradiance is a portion of the sun's collimated beam unmodified by the atmosphere. Like all technologies, CPV does have its setbacks. In order to exploit the direct sunlight, the module must continuously track the sun with high accuracy since the modules have a narrow light acceptance angle, which adds an extra cost and mechanical components that are subject to failures. A large variation in the sun's spectrum depending on location and time of day means the right MJSC is critical to minimize the spectral losses. Chromatic dispersion for refractive optics results in non uniform illumination of the MJSC, which is one of the major loss mechanisms in a CPV module. The large variation in ambient temperature can range from below freezing in the winters and about 40 °C during the summer for suitable CPV locations. The direct irradiance also heats the lens, further varying the temperature of the lens. Figure 1.4 shows the ambient and Fresnel lens temperature distributions for one year in Ottawa, Canada.

This thesis looks specifically into the effects of the operating conditions on the degree of chromatic abberation and non-uniformity in a CPV system. Current experimental methods

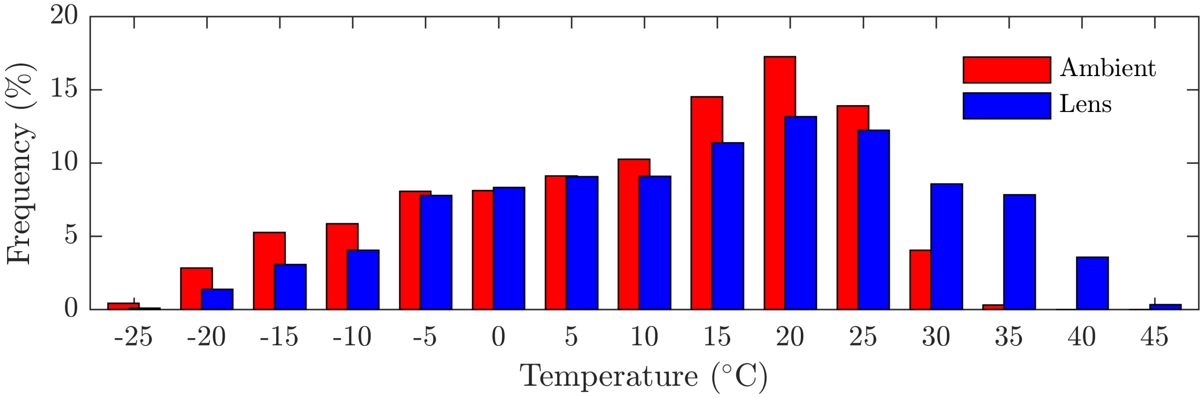

Figure 1.4: Distribution of annual ambient temperature and calculated[1] lens temperature of a Fresnel-based system for ground measured data in Ottawa, Canada.

of capturing an image of the profile only shows the spatial and not the spectral distribution. Since the performance of the MJSC is sensitive to both, seeing the full image of how the optic perform under different conditions is important. Therefore, this thesis will address the issues with current methods of imaging the optics of a CPV system, how manufacturing tolerances and temperature affects the performance through the development of an automated and controlled test-bench.

1.2 Thesis content

This thesis consists of six chapters. The first, which you are almost finished, introduces the current social dilemma wherein meeting the rising electricity demands with fossil fuel is unsustainable since they are harmful to the environment and depleting in resources. A positive note on our ever-developing society is the advancement in technology that has made for new forms of electrical generation possible by exploiting renewable energy sources. Although each source is plagued with their own issues, renewables are growing in popularity, with solar power being a dominate player in the energy mix. Specifically, the trends seen in previous emerging technologies show the potential for CPV in the energy industry.

The second chapter contains a detailed description of the solar resource and CPV system fundamentals. Starting with the sun, we will see a complete picture from its spectral distribution to how the different atmospheric components influence a local resource. Then, the principles of operation and losses in MJSC and concentrator optics are presented. Finally, a

---

[1] Refer to Chapter 5 for lens temperature calculation based on irradiance.

literature review focused on the loss mechanisms of CPV systems specifically, which includes chromatic aberration, spatial illumination, and lens temperature, is outlined. This section is a solid foundation of the theory that will be discussed in the subsequent chapters.

Chapter three is the first of three publications that make up the core material for this thesis and was published in *Optics Express* on the January 7^{th}, 2016. Due to the nature of the optical elements, dispersion prevents all the wavelengths to be focused at a single focal point, leading to spectral and spatial non-uniformities across the cell. Standard imaging detectors lack the spectral resolution needed to properly image the profiles of the layers in a MJSC. This article first discusses the issues with imaging optics, which leads into the necessary calibration procedures used to accurately generate a spectral map. With the calibrated output, the calculated values were accurate to within 3% when compared to electrical measurements of subcell isotypes. It finishes with a case study that shows how the experimental technique can characterize the effects of lens temperature on CPV systems. This chapter provides a full picture of an experimental technique that had yet to be seen in the literature.

Chapter four is a detailed article of the results presented at CPV-12, which is a specialized international conference in the CPV field where the proceedings were peer reviewed and accepted in the *AIP Conference Proceedings* on September 1^{st}, 2016. This paper shows the influence of lens temperature with an emphasis on the profiles for the top and middle layers of the MJSC in a CPV system. These preliminary results shows the degree that temperature can influence different optics and is the motivation for the detailed journal articles in chapter five.

Chapter five is the third journal publication that discusses the issues with three generations of CPV architecture. The systems compared are a silicone on glass primary lens without a secondary optic, a polymethylmethacrylate primary lens with a secondary optic, and a 4 Fresnel-Köhler two-stage design. Under field operation, the CPV system is subject to a variety of conditions that may alter its performance including, but not limited to, alignment, cell to primary distance, and lens temperature. With the experimental technique developed, a detailed analysis shows the isolated effects of the aforementioned conditions on the irradiance profile of the systems. Included is a system optimization study to show how lens temperature can impact the annual energy yield and efficiency based on both ground and satellite datasets. This article shows that CPV is making progress in mitigating the effects of different operating conditions; however, there is still room to improve in order to generate confidence in the technology.

The final chapter provides a summary of the results seen in this thesis. Furthermore, it recaps the advancement in CPV industry, suggestions on where research is needed, and lists the necessary issues and future work to improve the experimental technique.

Chapter 2

Basics and literature review of concentrator photovoltaic

2.1 Fundamentals

The sun is a star at the center of the solar system that provides the earth with an abundance of energy on a daily basis that is used by nature and society. It is critical to first understand the sun as a resource of energy and then how a CPV system converts that energy into clean electricity. This section will discuss the key parameters of the solar resource, the basics of an MJSC, the different generations of concentrator optics in CPV, and a literature review of the main loss mechanisms in CPV.

2.1.1 The solar resource

Outside of the earth's atmosphere, the average total solar irradiance is 1366.1 W/m^2 based on 24 years of measured satellite data [B - 4]. The earth's orbit draws out an elliptical pattern on a horizontal plane through the middle of the sun. The eccentricity of the earth's orbit results in a yearly variation with the two extremes in January and July when the earth is closest and furthest from the sun, respectively. For example, in 2015 the annual fluctuation of the irradiance at the surface of the atmosphere was 6.8% with 1414.0 W/m^2 and 1320.5 W/m^2 that corresponds to +3.5% and -3.3% from 1366.1 W/m^2.

The electromagnetic spectrum describes the energy of light as a function of its wavelength and all objects with a temperature above absolute zero, 0 Kelvin (K), emit radiation. The sun, in particular, is a sphere with a surface area of 6.09×10^{12}km^2 and effective temperature of 6000 K. Fusion of hydrogen atoms into helium results in a 3.8×10^{20} MW isotropic broadband radiation source. At the exterior of earth's atmosphere, the radiation energy intensity has decreased in proportion to the inverse of the distance squared from the source. The irradiance profile of the sun is similar to a blackbody, which is a perfect emitter and absorber governed by Plank's distribution [B - 5].

Figure 2.1 shows the blackbody radiation profile from 4000 K to 6000 K is shown at 150M km from its source, the mean earth sun distance. The visible band is shown to provide a reference to where the ultraviolet and infrared are, which is below and above the visible, respectively. As the temperature of the blackbody increases, the central frequency increases. Furthermore, the profiles of the blackbody is compared to the extraterrestrial solar spectrum. In reference to figure 2.1, 47% of the total sun's intensity is emitted within the visible region, 46% in the infrared region, and the remaining 7% in the ultraviolet.

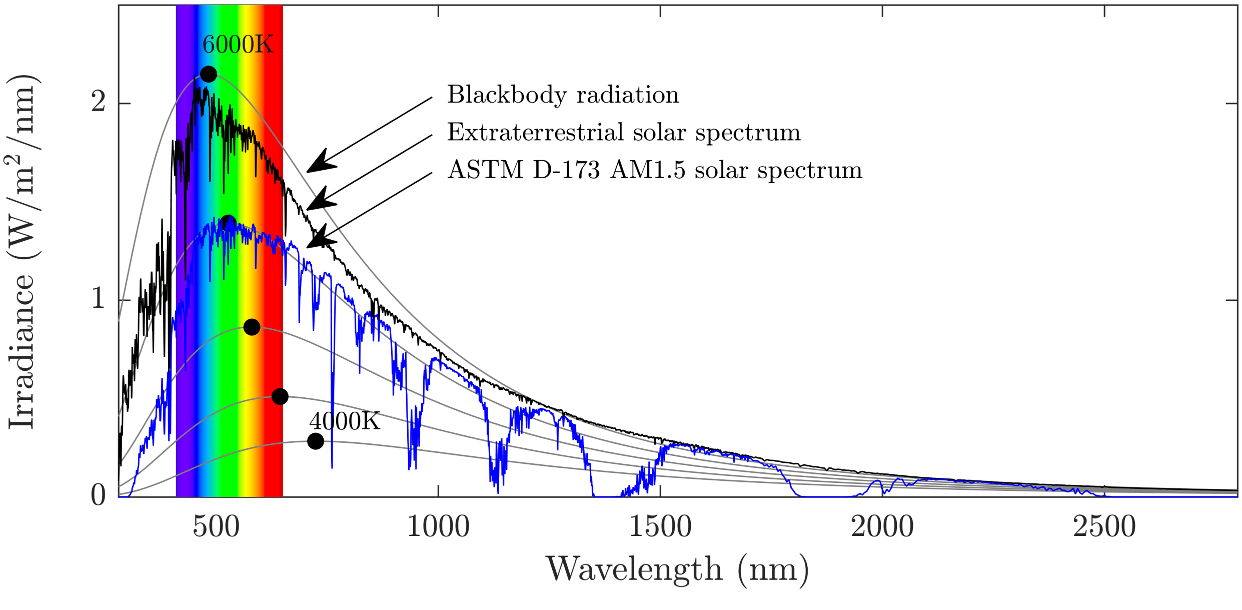

Figure 2.1: The blackbody spectra from 4000 to 6000 K at one astronomical unit away from the emitter source. The extraterrestrial solar spectrum can be approximated to the blackbody with a surface temperature of 6000 K. The ASTM D-173 AM1.5 is a reference solar spectrum for photovoltaic comparison, it's reduced from the extraterrestrial spectra by the photon-atmosphere interactions.

As light propagates through the earth's atmosphere, the spectrum is modified by the atmospheric constituents where the light is scattered and absorbed by molecules, aerosols, and clouds. As a result of the photon-atmosphere interaction, the incident solar radiation is broken down into three. The direct normal irradiance (DNI) is the portion of the sun's collimated beam unmodified by the atmosphere. The diffuse horizontal irradiance (DHI) are the photons at the earth's surface that have been scattered from the direct beam into random paths, creating an isotropic illumination to an observer. The global horizontal irradiance (GHI) is the total irradiance on a horizontal surface equivalent to the normal component of the DNI plus the total DHI. Each component will have a unique irradiance distribution that changes throughout the day depending on the composition of the atmosphere. Figure 2.1 shows the standard solar spectra, ASTM solar spectrum, where the energy lost reduces the extraterrestrial by 468.50 W/m^2 or 34.55% relative. The Figure 2.2 shows how the atmosphere interacts with the solar irradiance.

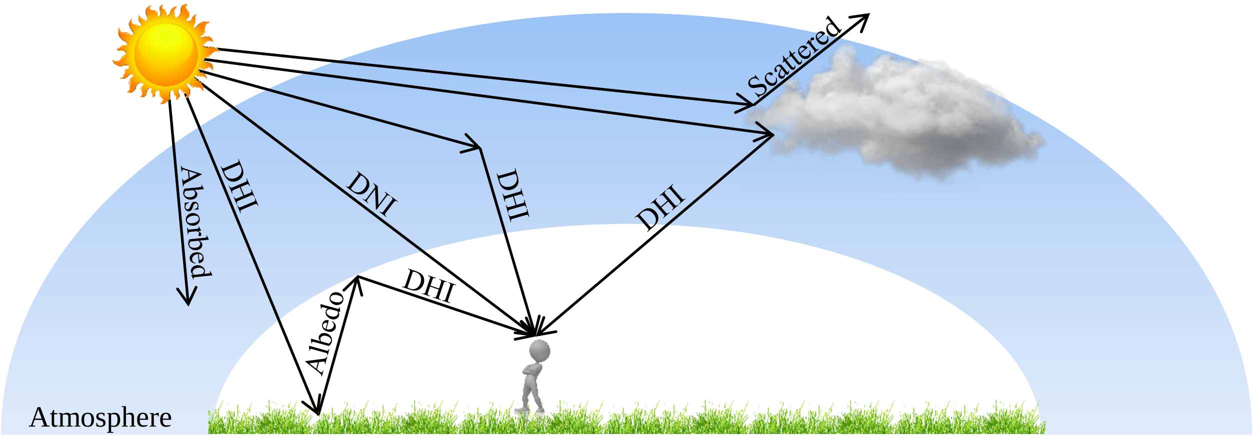

Figure 2.2: The effect of the atmosphere, clouds, and albedo on the components of the solar irradiance. The DNI is the unaffected direct light from the sun reaching the observer. The DHI is a isotropic source to an observer created by the reflections of the solar irradiance within the atmosphere, clouds, and ground.

The amount of attenuation of the solar spectrum is dependent on the density and path length, or air mass, that the light propagates through. The air mass is defined as the path length normalized to the shortest possible path length relative to the observer. The air mass is calculated from:

$$airmass = \frac{1}{\cos\theta} \tag{2.1}$$

where θ is the zenith angle, one of the two angles used to describe the location of the sun in the sky to an observer that are defined within the solar co-ordinate system for a local horizontal plane.The zenith angle describes the height of the sun and is measured from the zenith, the normal vector of the horizontal plane, to the sun.

Figure 2.3 shows the relationship between the sun's elivation angle, 90 minus the zenith angle, for a day. The air mass remains stable for elevation angles greater than 10°; beyond this point there is significant absorption and reflection by the atmosphere, which is why there are more colourful skies at sunrise and sunset. The azimuth angle is the compass direction of the sun and is measured from due north in the eastward direction. To an observer on earth, the sun traverses from east to west at a speed of 15°/hr from sunrise to sunset.

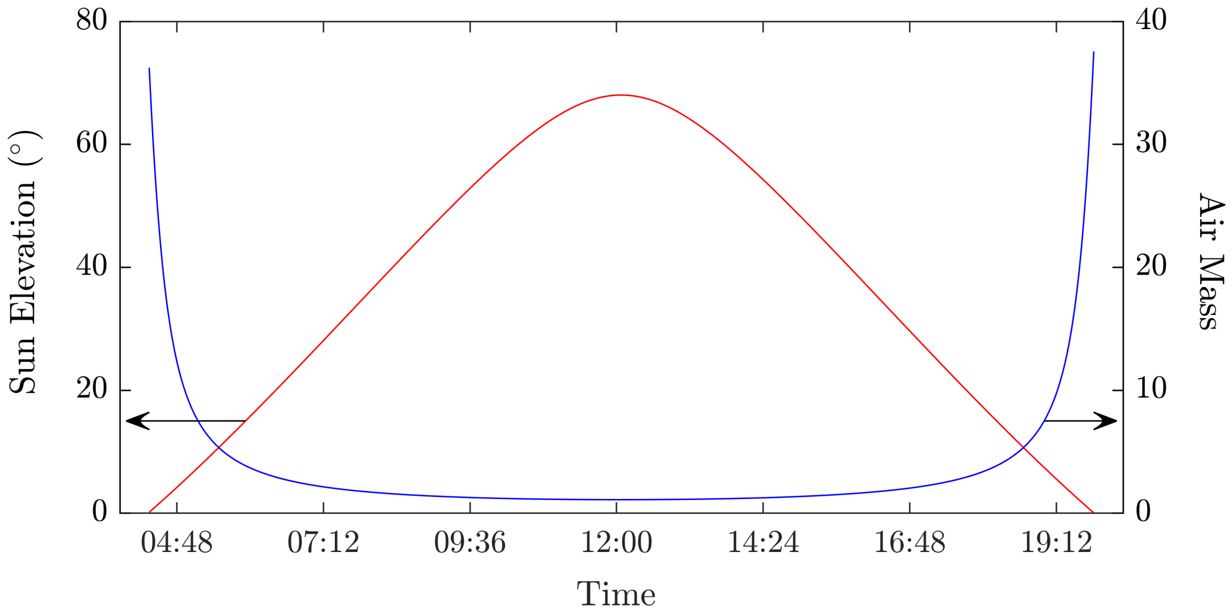

Figure 2.3: The elevation and air mass as a function of the day on the summer solstice.

The earth's orbit about the sun leads to seasonal variations. The height which the sun reaches is dependent on the declination angle, or how tilted the earth is with respect to the sun. Figure 2.4 shows the declination angle that measures the tilt of the earth with respect to the horizontal plane through the celestial sphere and governs how high the sun will be for a specific latitude. Seasonal variation results in a maximum declination angle of 23.45°at the summer solstice and a minimum angle of -23.45°on the winter solstice. The equinox occurs with a declination angle of 0 and the day and night are the same duration. In the literature, the exact location of the sun can be computed with a sun position algorithm that takes into consideration the observer's longitude, latitude, and elevation to return the solar zenith, azimuth, sunrise, and sunset [B - 6].

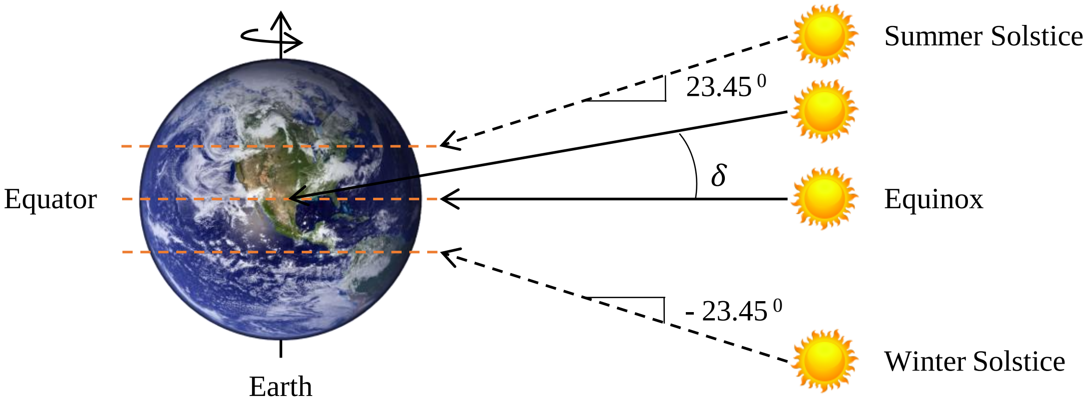

Figure 2.4: The declination of the sun at the equinox, summer and winter solstice, and for an arbitrary day during the summer.

Along with the air mass, another important atmospheric parameter is the aerosol optical depth. The aerosol optical depth is the measure of aerosols distributed within a column of air from the ground surface to the atmosphere. The Ȧngström parameters describe the size distribution of the aerosols and can either be measured or derived from the aerosol optical depth over a specific spectral range. Values of α close to zero indicates coarse particles and larger values indicates fine particles. Although this section does not include all the effects of the atmospheric constituents on spectrum, it has been studied and further information can be found in articles [B - 7, 8, 9, 10] and textbooks [B - 5, 11].

2.1.2 Multi-junction solar cells

A MJSC is a series-interconnected stack of semiconductor junction device where each layer harvests a different band of the solar spectrum. MJSC have been researched since the 1970's with efficiencies continuously climbing to date. Now, world record cell efficiency of 46.0% and 44.4% for quadruple- and triple-junction solar cells, respectively, have been obtained [B - 12]. Furthermore, MJSC are the motivation for CPV systems since inexpensive optical materials concentrate light on to smaller area to further increase efficiencies.

Three properties used to characterize the performance of solar cells are the short-circuit current density (J_{sc}), open circuit voltage (V_{oc}), and fill-factor (FF). The J_{sc} and V_{oc} are the maximum current density and voltage that can be extracted from an illuminated cell. The power is 0 for both the J_{sc} and V_{oc} since the voltage and current are 0, respectively. The fill factor then describes the maximum power of the cell and is calculated as

$$FF = \frac{J_{mp}V_{mp}}{J_{sc}V_{oc}} \tag{2.2}$$

where J_{mp} is the current density and V_{mp} is the voltage at the maximum power point of the IV curve. The output of a solar cell depends on both irradiance and temperature. Figure 2.5 (a) shows the effect of temperature on the IV curve of a solar cell where the I_{sc} slightly increases, the V_{oc} decreases linearly. The maximum power point, marked by (V_{mp}, J_{mp}), will decrease with temperature due to the V_{oc}. Figure 2.5 (b) shows the effect of increasing the irradiance on the IV curve where we see the J_{sc} increases linearly while the V_{oc} increases logarithmically. Under these conditions, the maximum power will increase. The efficiency (η) is a measure of a solar cell's ability to convert incident power,

$$\eta = \frac{I_{sc}V_{oc}FF}{P_{in}} \tag{2.3}$$

where P_{in} is the input power in W/m^2.

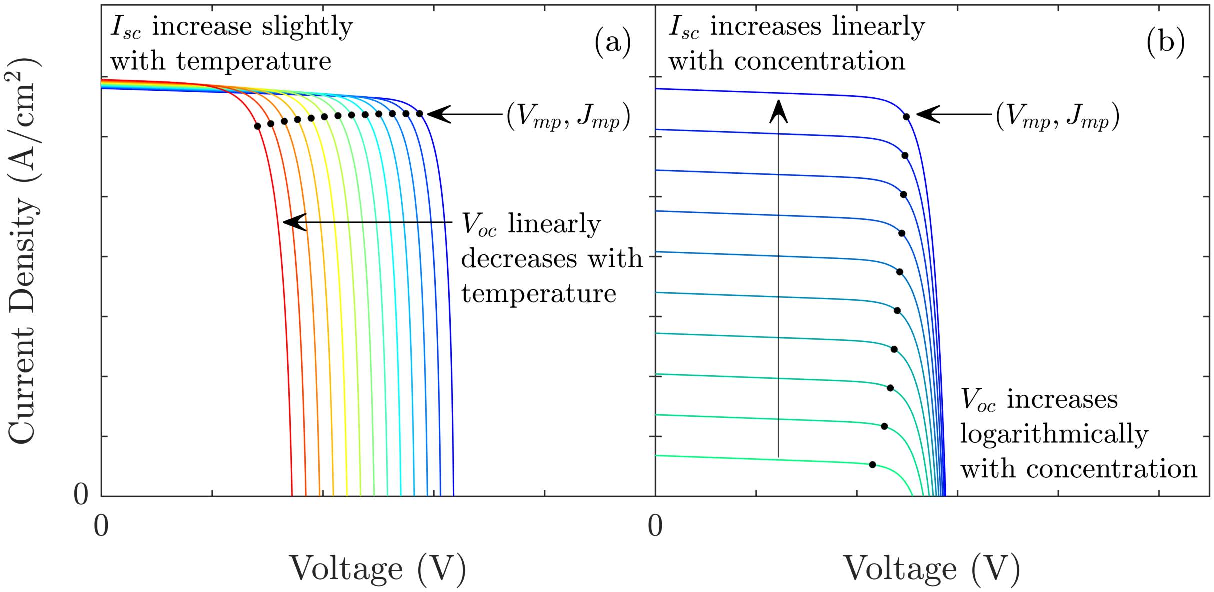

Figure 2.5: (a) The effect of temperature on the IV curve of a solar cell. (b) The effect of the irradiance on the IV curve of a solar cell.

The common denominator in all solar cells is the *p*-*n* junction where electrons can be extracted by the electric field formed by the exposed positive and negative ion cores when a *n*-type and *p*-type material are joined.

An MJSC consists of two or more stacked *p*-*n* junctions, or subcells, and are connected by a tunnel junction. A simplified MJSC structure is illustrated in figure 2.6 where sunlight is incident on the antireflection coating layer. The tunnel junction is a critical layer that uses tunnelling, a quantum mechanism phenomenon, to allow the flow of electrons between the layers.

The tunnel junction electrically connects the subcells of the MJSC in series. The total current is then limited by the subcell that generates the least amount of current. The MJSC is connected to an exterior circuit by the top and bottom contacts where the top contacts have a grid pattern, different per cell design, to allow light to pass and interact with the cell.

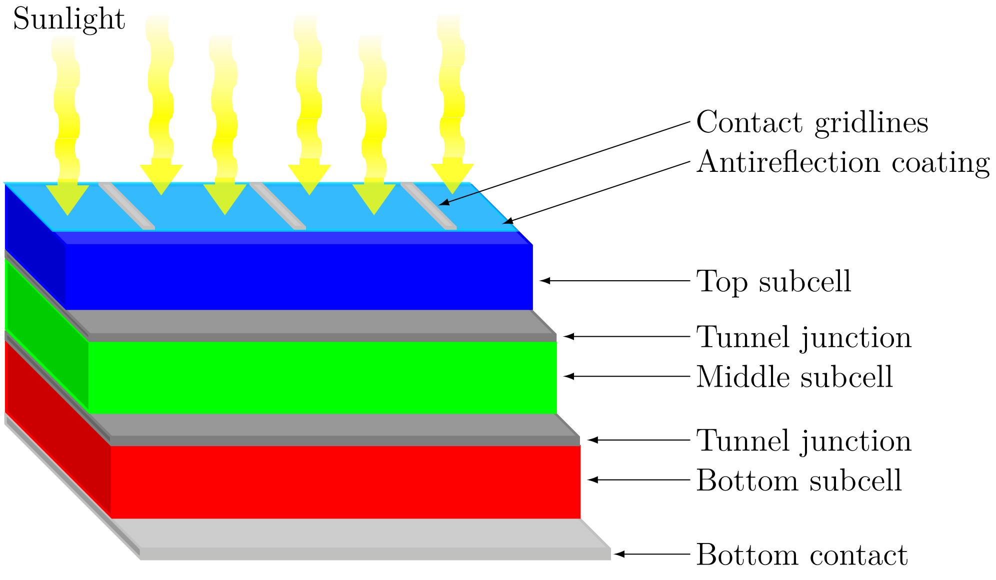

Figure 2.6: Sunlight incident on a triple junction solar cell structure. The tunnel junctions connect each layers allowing the flow of electrons once absorbed. The contact grids is the connection to the external circuit where the top contact has a gridline geometry to allow light to enter into the cell. The antireflection coating reduces the Fresnel losses as the photon strike the surface of the solar cell.

In principle, photons incident on a semiconductor material will either be reflected, absorbed, or transmitted. Both reflection and transmission are considered loss mechanisms in a solar cell system. The former is governed by the Fresnel equations that describe the flow of energy between light incident on a media of different refractive indices. In a semiconductor material, an electron can hold one of two states. Either bonded in the valence band, or free in the conduction band. The band-gap energy is the difference in potential between the states. Therefore, the bad gap is the minimum change of energy required to excite an electron from the valence band to the conduction band.

The energy of an incident photon can be categorized into three with respect to the band-gap energy of the semiconductor material. A photon is transmitted through the material when its energy is less than the band-gap of the material. The ideal scenario is when the photon has the same energy as the band-gap; there is then sufficient energy to absorb the photon and excite an electron to the conduction band with no thermalization losses. When the energy is greater than the band-gap, a third loss mechanism is introduced, since the excess energy absorbed in the transition is lost to thermalization as the electron will quickly thermalize down to the band-gap energy level.

The thermalization losses put a fundamental limit on the conversion efficiency of all solar materials. Without concentration, the detailed balance calculation of the optimal single and triple band-gap combination are 32.5% and 49.7%, respectively [B - 13]. The theoretical efficiencies of the MJSC further increases under concentration. If we compare a Si solar cell, bassically a single junction MJSC, the limit for the MJSC is higher due to its ability to reduce the thermalization and transmission losses.

Figure 2.7 shows the losses of an MJSC and a Si solar cell. The colour coded areas show the absorbed spectral irradiance and the black area is the total thermalization and transmission losses. In an MJSC, the subcells are stacked from top to bottom in decreasing band-gap energy. The most common MJSC is the lattice-matched triple junction solar cell grown on germanium substrate with a gallium indium arsenide and gallium indium phosphide middle and top subcells (InGaP/InGaAs/Ge). In reference to figure 2.7(a), the photons absorbed by the top subcell, shown in blue, photons with a wavelenght less than 670.18nm, 1.85 eV, relax to the band-gap and contribute to thermalization losses. The further the photon wavelenght is from the band-gap, the greater the thermalization loss, as seen in 2.7. The photons below the band-gap energy are transmitted to the ensuing subcell.

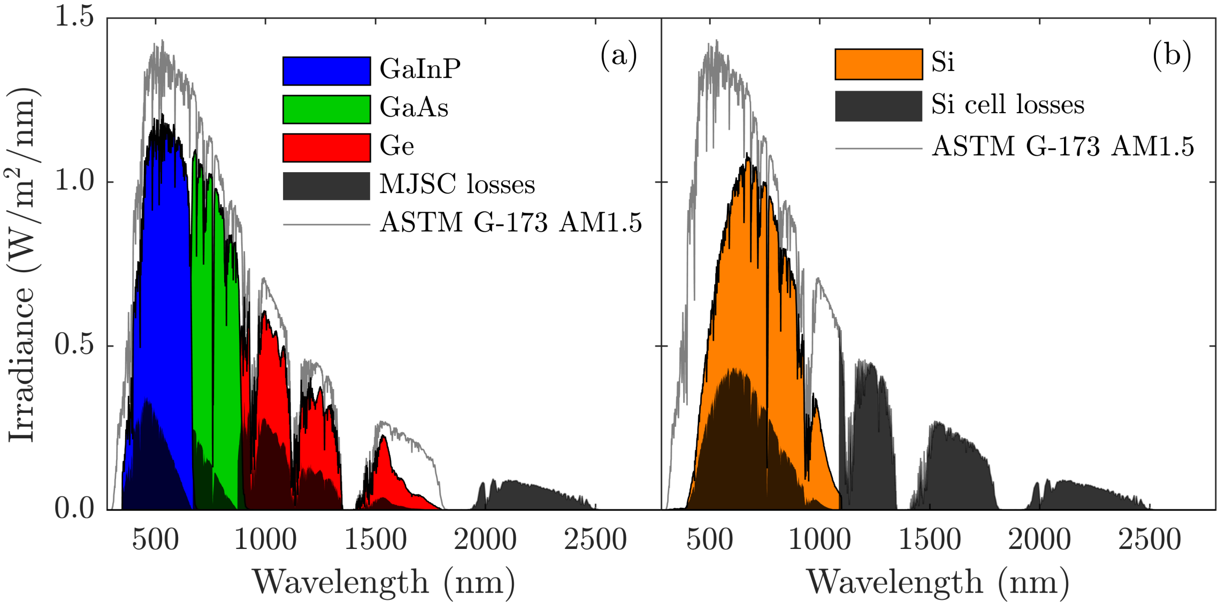

Figure 2.7: MJSC absorbed spectral irradiance of a multi-junction solar cell (a) and Si solar cell (b) as a function of wavelength under the ASTM spectrum. The top, middle, and bottom subcells are shown in blue, green, and red, respectively, and the Si solar cell in orange. The thermalization and transmission losses are represented as the black areas under the absorption spectra.

The same interaction will occur in the middle and bottom subcells, except the cutoff wavelengths are 873.12nm and 1850.51nm, respectively. This cascade effects helps reduce the energy lost to thermalization since more photons are absorbed closer to the band-gap edge. The losses under the ASTM G-173 AM1.5 spectrum are 190.51 W/m^2 for the MJSC and 331.14 W/m^2 for Si solar cell, which is 21% and 37% of the total incident radiation, respectively. As the number of subcells increase, there will be less thermalization loss.

The famous solar cell efficiency road map published every year by NREL can be seen in figure 2.8 on the next page. The chart groups all the latest advancements in efficiency for the different types of solar cell technologies (MJSC, Si, ThinFilm, Organic, etc.). It is clear that MJSC efficiencies, in purple, are continuously rising, whereas Si single junction cells have plateaued, in blue. The advantage of an MJSC is its ability to harness a large spectral range for more efficient transformation of sunlight to electricity than traditional single junctions.

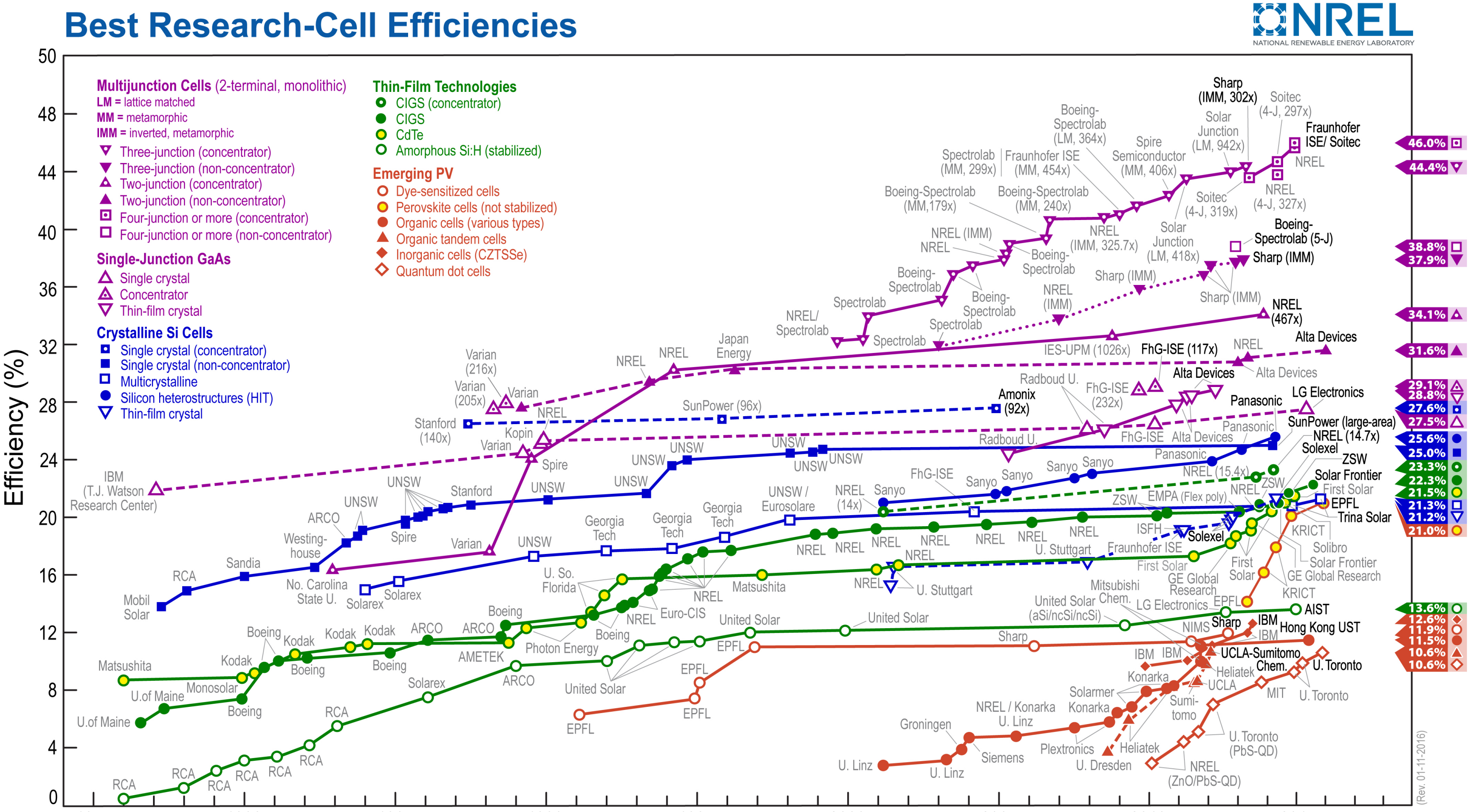

Figure 2.8: Record efficiencies of solar cell technologies from 1975 to 2016 [B - 12].

The three types of triple junction solar cells are current-matched, metamorphic, and inverted metamorphic. The traditional is the current-matched, where materials are chosen based on matching the lattice constants to reduce crystal defect during production. For the metamorphic and inverted metamorphic, there is a buffer layer that gradually changes the lattice constant. This transition layer is found between the bottom and middle subcell, while the top and middle are still lattice matched. This allows for tunability, reducing the thermalization losses. This also changes the bottom subcell to a lower bandgap to reduce the transmission losses.

2.1.3 Concentrator optics

The continuous advancement in MJSC designs and efficiency are matched by new concentrator designs for CPV systems. These concentrators can be categoried as either refractive or reflective and, in order to have a competitive levelized cost of energy with traditional PV, the concentrations must be greater than 500 suns (1 sun = 1000 W/m^2) [B - 15].

Figure 2.9 shows an example of the three types of concentrators. A refractive concentrator typically uses a variation of the Fresnel lens since its rotational symmetric facets allow the system to be compact, less absorptive, and cheaper. A reflective concentrator will hire a mirror that sharply focuses the incident rays to a point. Reflective concentrators have two

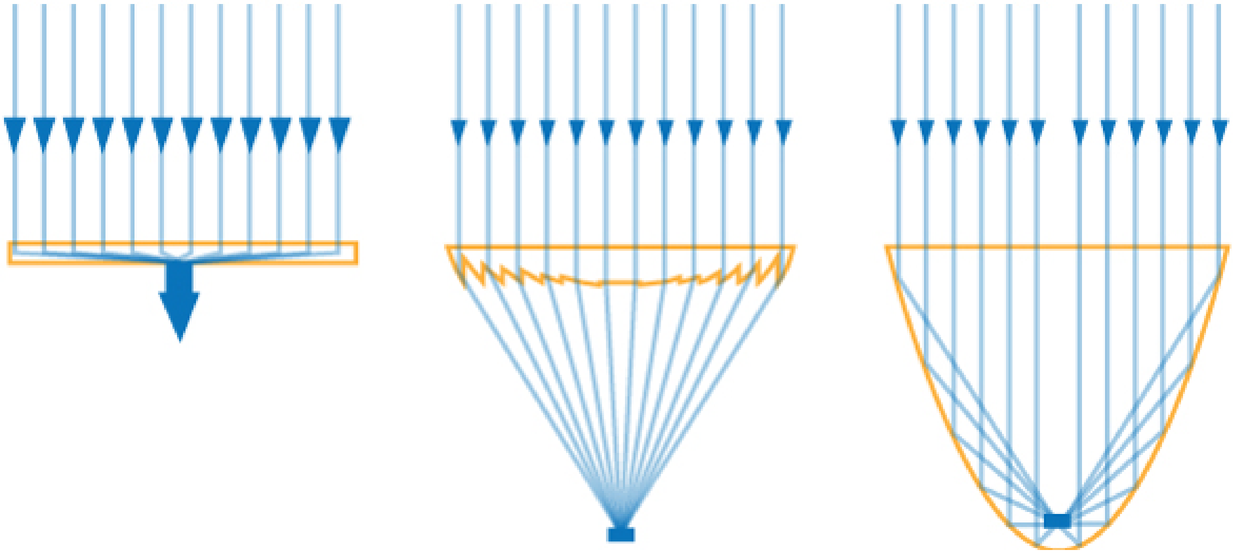

Figure 2.9: Representation of optical typologies for a light-guide solar optic, Fresnel lens, and reflective concentrator photovoltaic systems, from left to right [B - 14].

distinctive advantages to the refractive optics. First, there is no inactive area, unlike the Fresnel lens which has sections between the adjacent facets are inactive, resulting in a lower total exit area. Secondly, as the light never changes material, reflective concentrators do not suffer any chromatic dispersion, a loss mechanism that will be discussed for refractive optics. However, reflective concentrators have smaller acceptance angles, suffer from *coma*, which is an optical aberration causing a strong non-uniform magnification across the MJSC, and have limited concentration levels, making refractive concentrator the better option for CPV. Another concentrator design, referred to as a light-guide solar optic uses total internal reflection to guide light, and has shown potential since it can achieve a concentration ratio above 1000 suns while drastically reducing the size of the module.

Regardless of the refractive concentrator's design, the light changes propagation mediums, where a portion of the energy will be lost due to reflection and absorption. Figure 2.10 shows the optical transfer functions for a polymethylmethacrylate (PMMA), light-guide and a Fresnel-based CPV system. The optical transfer function describes the transmission of light as a function of its wavelength. It is a value between 1 and 0, as shown on the right axis, that describes the portion of energy transmitted at a specific wavelength. The shaded

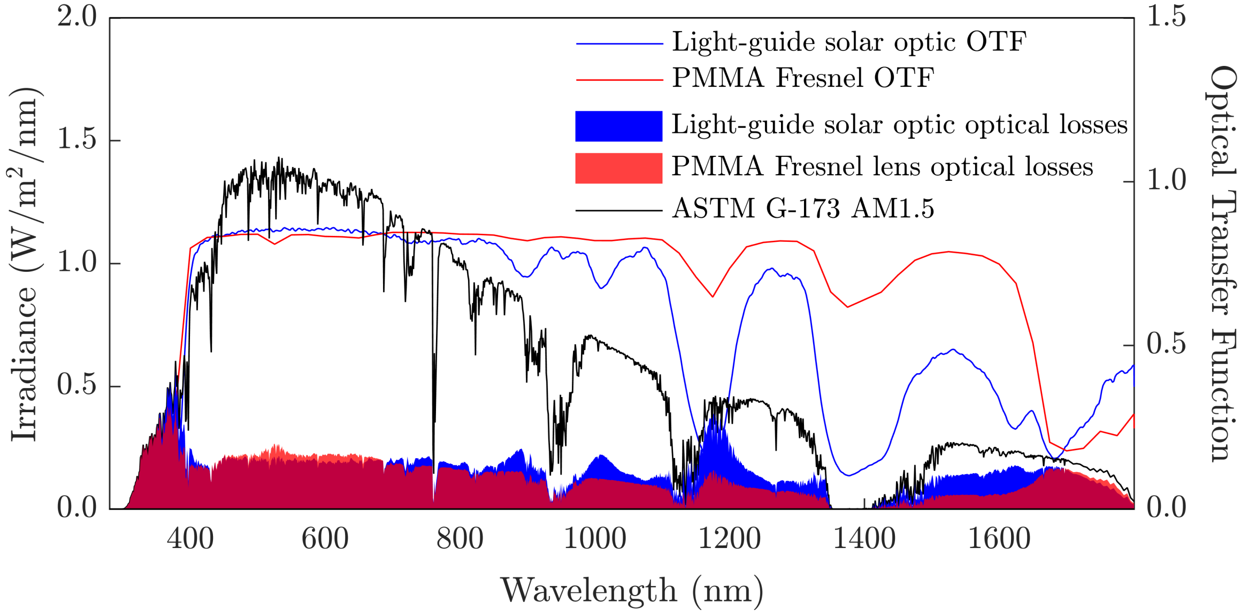

Figure 2.10: Optical losses of a light-guide solar optic and Fresnel system under the ASTM reference spectrum. The optical transfer function, right axis, shows the transmission profile for the two systems.

areas under the optical transfer function is the total loss in irradiance due to the optics when illuminated with the ASTM spectrum, black curve. It is evident that even though these systems have the same material, there are higher losses in the light guide optic above 800 nm. This can lead to a limitation in the middle and bottom subcell current generation. The additional losses are due to the path length, which is higher in the light guide optic. Under the ASTM spectrum, which has a total power of 900 W/m^2, the optical losses are 265.67 W/m^2 and 217.23 W/m^2 for the light-guide and Fresnel lens, respectively. This example is a simple case of the difference between two optical architectures with the same material. However, in reality, there are both different materials and architectures to choice from.

To date, there have been three distinct generations of CPV optical designs. The first is a Fresnel lens without a secondary, shown in figure 2.9. It has stood the test of time since it is simple and compact. CPV companies, such as Soitec, use a SoG Fresnel architecture with a triple-junction solar cell for their modules. The issue with the first generation is a high degree of non-uniform flux distribution and small acceptance angle, both improved by placing a secondary on the MJSC.The introduction of a non-imaging secondary optic marks the second generation in CPV optical designs. Typical secondaries used by CPV companies are either a spherical dome, reflective truncated pyramid, or refractive truncated pyramid. These secondaries are designed separately from the primary, the primary is assumed to be a Lambertian source at entry of the secondary. Finally, the most recent generation improves the optical performance since the secondary and primary are designed together. A commercialized product is the 4 Fresnel-Köhler concentrator, which has a four-fold primary and secondary optics. This design divides the incident rays into four Köhler channels. By reducing the field of view for each channel, effects on the primary are also reduced as each channel has a smaller contribution since they are individually superimposed onto the cell. Another design within the third generation is the light-guide solar optic, the system was designed and implemented by Morgan Solar. The optic is designed such that the optical path of the light always remains within one material and has a geometric concentration of 1111.

Comparison of concentrator architecture system performance are based on acceptance angle and geometric concentration. From a design perspective, a concentrator with high geometric concentration and relaxed tolerances is ideal. However, there will be a trade-off since the ideal conditions are difficult to achieve due to fundamental constraints on the optical design. A merit function for copmaring different concentrators designs is the acceptance angle product (CAP), calculated as,

$$CAP = \sqrt{C_g}\sin(\alpha) \tag{2.4}$$

where C_g is the geometric concentration and α is the acceptance angle, which is the exact angle at which 90% of the total power is still collected. The upper bound of the CAP is less than or equal to the refractive index of the material, also known as the Étendue theorem [B - 16]. Since CPV is still in its development stage, there is minimal reliability data available to compare the different generations. However, it has been shown that the system with the highest CAP will have a better potential [B - 16]. For example, if we were to compare a silicone on glass (SoG) to a PMMA Fresnel lens, with the same concentration and acceptance angle, the SoG would win since it has a refractive index around 1.51 and PMMA's is 1.49. Other advantages that an SoG primary has are its rigidity, long-term reliability, and more precise manufacturing tolorences. This comparison is a simple case; in reality, there are numerous different types of optical designs and materials, therefore the CAP becomes a more useful tool.

Figure 2.11 show the attainable CAPs of six different CPV systems that were compared by Gombert et al. [B - 16]. They have been colour-coded to match the three generations discussed in the previous paragraph. The advancement of optical designs has led to an relative increase of 250% in CAP from the SoG Fresnel design of the first generation. Within each generation, we see a range of different values. The leading technologies are the SoG primary without a secondary, the refractive truncated pyramid, and 4 Fresnel-Köhler with CAP values of 0.18, 0.48, and 0.63, respectively [B - 16].

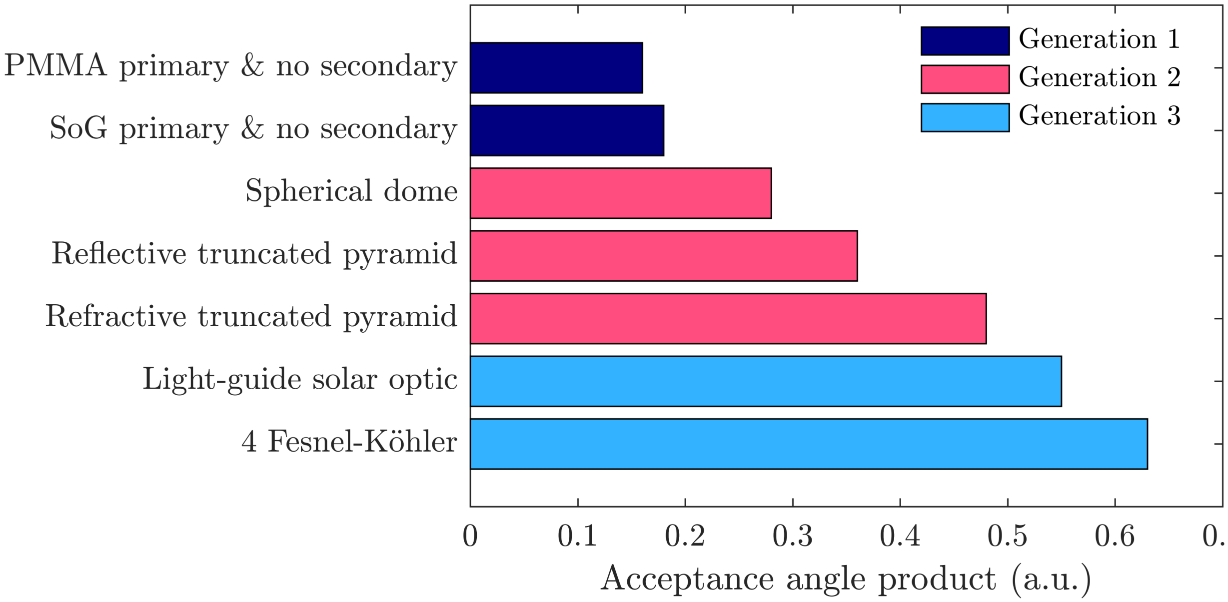

Figure 2.11: The acceptance angle product, CAP, compared for the three generations of concentrator photovoltaic optical designs, adapted from [B - 16].

2.2 Loss mechanisms

The dispersion of the optical components results in a non-uniform, both spatial and spectral, distribution of light across the different subcells, reducing the efficiency of an MJSC. The effect on the MJSC performance has been studied extensively in the CPV literature and the main results are summarized in this section to provide a clear understanding of their cause and effects.

2.2.1 Chromatic aberration

Chromatic aberrations occurs when an optical element is unable to focus all the wavelengths to a common focal plane. In an MJSC, each subcell will have a non-uniform spectral profile. Excess current can flow laterally within the subcells to compensate, but otherwise it's wasted through recombination, leading to poor cell performance.

In Fresnel optics, as light propagates through the dispersive medium, the optical path length is dependent on the incident wavelength. Therefore, as the rays exit the optic, they converge at different points in space, leading to axial and lateral aberrations. A result of the different refractive indices that depend on the wavelength of the light. Figure 2.12 shows the chro-

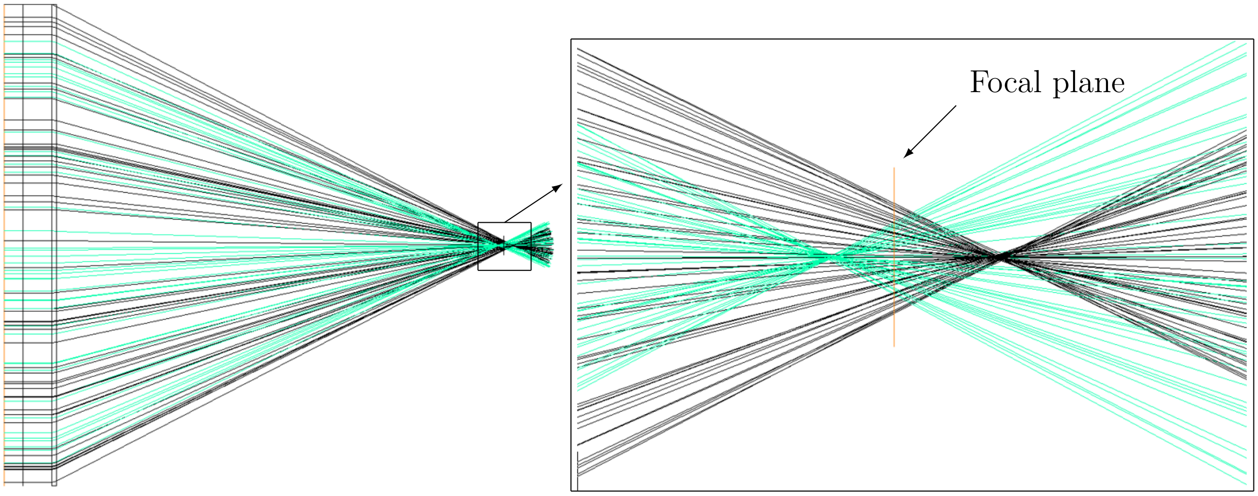

Figure 2.12: Ray-tracing diagram of a Fresnel lens at 500nm and 1000nm. The chromatic aberration can be seen when focusing in on the focal plane where the convergence of shorter wavelength are before the focal plane and the longer wavelengths are beyond the focal plane. The placement of the focal place is optimized for maximum power.

matic aberration of a Fresnel lens with a ray-tracing diagram at 500nm, green, and 1000 nm, black. The two wavelengths seem to converge at the focal plane, which to the eye resembles a bright white spot. However, when zoomed in on the focal plane, it is evident that the 500 nm and 1000 nm are not focused at the same point, but before and after the focal plane, respectively. Additionally, the amount of dispersion is proportional to the thickness of the lens [B - 17].

The cell to primary distance plays a role in how much chromatic aberration will be present in the system. As the cell moves towards the primary, there is a higher concentration of light in the top subcell region. Consequently, the middle subcell will limit the MJSC since there is a reduced concentration in its spectral range. Cotal et al. [B - 17] compared the effects of chromatic aberration on fill factor and efficiency of a 1 cm^2 and 0.306 cm^2 lattice matched triple junction cell at different primary to cell distances. The effects on the smaller cell were less pronounced. This is a result of the beam waist to cell size: when the cell is smaller than the beam waist, the lateral aberrations have a larger effect on performance.

P. Sharma [B - 18] modelled the effect of chromatic aberration for the four-junction cell. The optical system was a PMMA Fresnel lens primary with a BK7 truncated pyramid homogenizer secondary. The difference in the four images seen in figure 2.13 demonstrates the chromatic aberration in the systems. The same MJSC was compared under a uniform irradiance profile and had an increase in absolute efficiency of 3% [B - 18]. The experimental results shown by Victoria et al. [B - 19] agree with the modelling results of Sharma. By changing the cell to primary distance, under various inhomogeneous profiles there was a drop of 5% to 10% in absolute efficiency.

Lateral current flow patterns in an MJSC, due to chromatic aberration, can have an impact on the short circuit current. García et al. [B - 20] used a distributive cell model that included lateral conductive paths the study current spreading within the subcell layers. The chromatic aberration was simulated by varying the intensity with a Gaussian spatial intensity profile on the middle subcell. Fundamentally, the excess photocurrent produced in the middle subcell can either increase or reduce the overall short circuit current of the cell. The results showed an abrupt effect once a certain sheet resistance is reached. The cross section voltage of the subcell increases with the sheet resistance until the open circuit voltage is reached, the recombination increases exponentially, blocking the lateral flow of current and limiting the short circuit current. If lateral current from chromatic aberration can flow without resistance within the cell structure, the effects on performance can be reduced significantly.

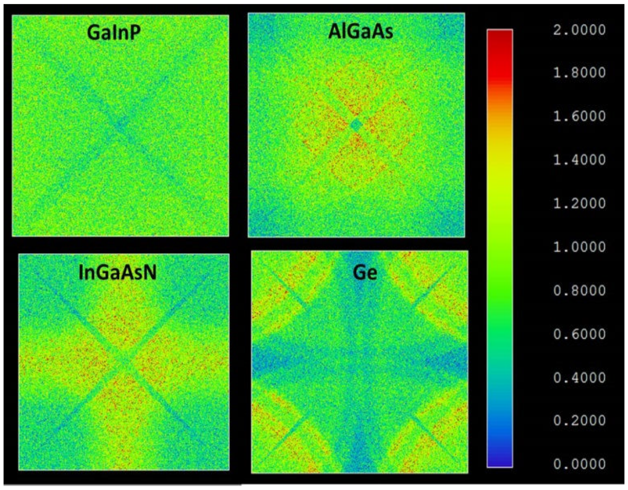

Figure 2.13: Irradiance profiles for each subcell in a four junction cell for first second generation CPV optics [B - 18].

2.2.2 Spatial illumination

Spatial non-uniformity of the flux distribution over the cell are introduced by the concentrators discussed in section 2.1.3. This non-uniformity adversely affects the efficiency of the device since high localized current densities increase the series resistance losses in top contacts of the MJSC. Furthermore, the tunnel junction limits the flow of current through the device when there is a surge of current generated within a subcell layer.

Optical-electrical modelling approaches can simulate the spatial distribution on an MJSC and can be used to optimize cell structures to mitigate the effects. A study by P. Sharma [B - 18] modelled a lattice-matched quadruple junction solar cell to optimize finger spacing under non-uniform illumination. In reference to figure 2.14, the system performance was modelled with a Gaussian distribution spatial illumination across the cell at different peak-to-average ratio. With an increase in the peak-to-average ratio, the optimized cell structure resulted in an absolute increase in efficiency of 0.9% and 1.8% under 1000 and 2000 suns, respectively. Studies [B - 21, 22, 19, 23] also use distributive cell models to study the electrical effects within an MJSC with results in the same order of magnitude as shown by P. Sharma.

Modelling systems provide foreseeable insight into what is happening within the cell, but it is also important to validate the models with experimental techniques. A comparative analysis was performed to isolate the optimal primary-to-cell distance for a bare cell, pyramid secondary, and dome secondary and show the effects of non-uniformities on MJSC performance

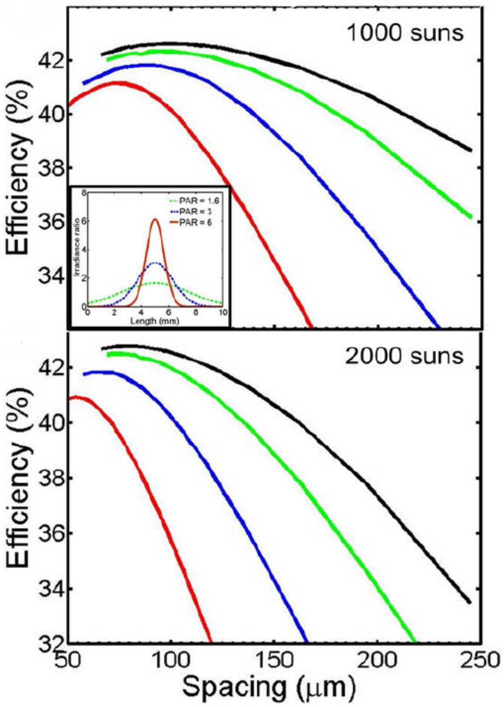

Figure 2.14: Efficiency as a function of grip spacing at 1000 suns for uniform (black) and PAR of 1.6(green), 3(blue), 6(red) irradiance profiles [B - 18].

by Victoria [B - 24]. In comparison, at close distances, all three have their respective worst-case scenario. As the cell is distanced, the focal points shift to higher wavelengths, affecting the current balance in the MJSC. The bare cell and dome secondary have a clear optimal location, whereas the pyramid has a uniform distribution. Out of the I_{sc}, V_{oc}, fill factor, and efficiency, the fill factor of the bare cell showed the greatest sensitivity. For the same distance, the fill factor is reduced by 15% when the concentration is increased since there is also an increase in spatial non-uniformity compared to less than 2% for the other two [B - 24]. Furthermore, the optimal measured and simulated cell distance differed, demonstrating the importance of experimentally optimized systems, which results in higher efficiencies.

All of these approaches, and others within the literature, demonstrate that due to non-ideal optical properties of the concentrators, spatial non-uniformity is introduced and reduces the electrical performance. Current practices of primary to cell distance, finger spacing, and different secondary show different possibilities to reduce spatial non-uniformity.

2.2.3 Lens temperature

Suitable locations for CPV deployments can have ambient temperatures ranging from well below freezing during the winter to upwards of 40 °C in the summer. The irradiance incident on the module can further increase the temperature, in the order of 10 °C per 1000 W/m^2, while other factors such as wind speed can cool the lens. The two properties of the refractive optical materials making the lens dependent on temperature are the index of refraction and the coefficient of thermal expansion.

The refractive index is inversely proportional to temperature. The increase in temperature will then decrease the refractive index, thereby increasing the focal distance of the Fresnel lens. Since the cell to primary distance is fixed within a module, this will cause the blue light, top subcell spectral band, to be more focused onto the cell and will cause a loss in the infrared region, middle subcell band. One of the first studies was performed by Shullt et al. [B - 25], their simulations showed a decrease of 10% in short circuit current when the lens temperature was increased by 20 °C. Figure 2.15 shows the thermal effect on refractive index for SoG.

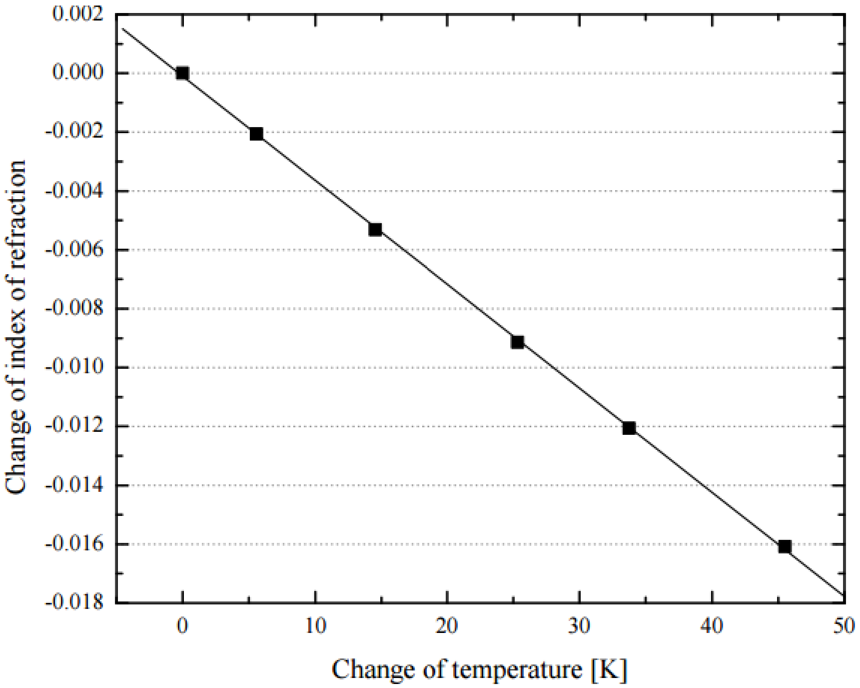

Figure 2.15: The measured effects if temperature on the index of refraction on for silicon on glass Fresnel lens [B - 25].

The coefficient of thermal expansion will causes a deformation in the facets of the Fresnel lens. For a SoG Fresnel lens, the rigid glass prevents the lateral expansion of the silicon, but the convex/concave deformation of the facets will affect the spot size and concentration of the light on the MJSC. Figure 2.16 is a schematic diagram of the deformation of a SoG Fresnel lens. The measurement technique discussed by Hornung et al. [B - 26] shows a decrease of 13% in concentration when the lens temperature is heated by 20 °C. Rumyantsev et al. [B - 27] showed a decrease of 8% in the optical efficiency when the SoG Fresnel is heated by 20 °C. The thermal coefficient of expansion of PMMA is more than two orders of magnitude higher than glass, which means it will also have lateral expansion, further decreasing the concentration and optical efficiency as seen in [B - 16].

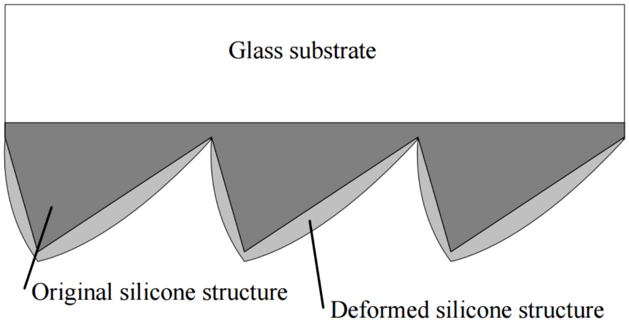

Figure 2.16: Visualization of thermal deformation of Fresnel lens prisms on a glass substrate when the temperature is increased [B - 26].

Chapter 3

New CPV characterization technique

3.1 Spectrally-resolved measurement of concentrated light distributions for Fresnel lens concentrators

3.1.1 Scope and contribution

The following publication describes the development and parameterisation of a test method that Dr. Besson and I developed in order to properly spectrally image the profiles of any refractive or reflective CPV optical architecture. This paper represents the first publication where this type of characterization technique, which improves previous attempts, was successfully used to characterize the irradiance profile to within 3% for a CPV optics performance analysis.

Other techniques and methods within the literature lacked the spectral resolution, accuracy, and versatility needed to image multiple CPV systems. The distinct difference and advantage was the combination of band-pass filters and a camera. In short, the system was built using a complementary metal-oxide semiconductor or CMOS camera, 12 band-pass filters with 50 nm full-width half maximum, an opal diffuser, and a thermal chamber. This allowed us to determine a 375 - 975 nm spectrum with a 10 μm^2 resolution. The test-bench was integrated into a module size solar simulator installed at the CAE-INES CPV research lab in France and fully controlled by a LabVIEW interface. The test system was used for a number of projects at CAE-INES and continues to be an extremely valuable tool since it gives the user an understanding of a systems optical response to different operating condition such as alignment and lens temperature.

Dr. Besson and I worked along side eachother for 10 months developing the experimental technique, building the systems, determining and measuring the calibration factors, and writing the publication. My major contribution was the design and building of the stand alone measurement system, which is capable of monitoring the lens temperature to capture and stitche the 12 images, one per filter, to give the irradiance profile a single operating condition, or any combination of lens temperature and alignment. Additionally, I developed the documentation that fully describes all the calibration factors used and full characteristics of element in system component, which was used for the base of the publication. This article was not used for Dr. Besson's thesis.

3.1.2 Publication

Pierre Besson, **Patrick McVey White**, César Domínguez, Philippe Voarino, Pablo Garcia-Linares, Mustapha Lemiti, Henry Schriemer, Karin Hinzer, and Mathieu Baudrit, "Spectrally-resolved measurement of concentrated light distributions for Fresnel lens concentrators," *Optics Express* **24**, 397-407 (2016).

Paper attached on the next page.

Spectrally-resolved measurement of concentrated light distributions for Fresnel lens concentrators

P. Besson,[1,5] P. McVey White,[2,6] C. Dominguez,[3] P. Voarino,[1] P. Garcia-Linares,[1] M. Lemiti,[4] H. Schriemer,[2] K. Hinzer,[2] and M. Baudrit[1]

[1] *CEA-LITEN, LCPV, INES, Le Bourget du Lac, France*
[2] *SUNLAB, Centre for Research in Photonics, University of Ottawa, Ottawa, Canada*
[3] *Instituto de Energía Solar, Universidad Politécnica de Madrid, Madrid, Spain*
[4] *University of Lyon, Lyon Institute of Nanotechnology, National Institute of Applied Sciences of Lyon, Villeurbanne, France*

Abstract: A test method that measures spectrally resolved irradiance distribution for a concentrator photovoltaic (CPV) optical system is presented. In conjunction with electrical *I-V* curves, it is a means to visualize and characterize the effects of chromatic aberration and nonuniform flux profiles under controllable testing conditions. The indoor characterization test bench, METHOD (Measurement of Electrical, Thermal and Optical Devices), decouples the temperatures of the primary optical element (POE) and the cell allowing their respective effects on optical and electrical performance to be analysed. In varying the temperature of the POE, the effects on electrical efficiency, focal distance, spectral sensitivity, acceptance angle and multi-junction current matching profiles can be quantified. This work presents the calibration procedures to accurately image the spectral irradiance distribution of a CPV system and a study of system behavior over lens temperature.

OCIS codes: (350.6050) Solar energy; (120.0120) Instrumentation, measurement, and metrology; (040.5350) Photovoltaic; (220.1770) Concentrators.

References and links

1. Fraunhofer ISE, Soitec, CEA-Leti, "New world record for solar cell efficiency at 46%: French-German cooperation confirms competitive advantage of European photovoltaic industry," [Press Release], Freiburg (2014). http://www.ise.fraunhofer.de/en/press-and-media/press-releases/press-releases-2014/new-world-record-for-solar-cell-efficiency-at-46-percent.
2. Fraunhofer ISE, Soitec, CEA-Leti, "Four-junction solar cell developped using Soitec's expertise in semiconductor materials sets new efficiency record of 38.9% for CPV module," [Press Release], Grenoble (2015). http://www.soitec.com/en/news/press-releases/article-1737.
3. J. Haysom, O. Jafarieh, H. Anis, K. Hinzer, and D. Wright, "Learning curve analysis of concentrated photovoltaic systems," Prog. Photovolt. Res. Appl. **23**(11), 1678–1686 (2015).
4. P. Sharma, A. W. Walker, J. F. Wheeldon, K. Hinzer, and H. Schriemer, "Enhanced efficiencies for high concentration, multijunction PV systems by optimizing grid spacing under nonuniform illumination," Int. J. Photoenergy **2014**, 1–7 (2014).
5. R. Herrero, M. Victoria, S. Askins, C. Domínguez, I. Antón, G. Sala, and J. Berrios, "Indoor characterization of multijunction solar cells under non uniform light patterns," in *CPV6 Conf. Proc.* (Amer Inst. Physics, 2010), pp. 36–38.
6. S. Kurtz, D. J. Friedman, and J. M. Olson, "The effect of chromatic aberrations on two-junction, two-terminal, devices on a concentrator system," in *Conf. Record of the 24th IEEE PVSC* (IEEE, 1994), pp. 1791–1794.
7. P. Espinet-González, R. Mohedano, I. García, P. Zamora, I. Rey-Stolle, P. Benitez, C. Algora, A. Cvetkovic, M. Hernández, J. Chaves, J. C. Miñano, and Y. Li, "Triple-junction solar cell performance under fresnel-based concentrators taking into account chromatic aberration and off-axis operation," in *CPV8 Conf. Proc.* (Amer. Inst. Physics, 2012), pp. 81–85.

#251636 Received 15 Oct 2015; revised 20 Nov 2015; accepted 22 Nov 2015; published 7 Jan 2016

8. M. Victoria, R. Herrero, C. Domínguez, I. Antón, S. Askins, and G. Sala, "Characterization of the spatial distribution of irradiance and spectrum in concentrating photovoltaic systems and their effect on multi-junction solar cells," Prog. Photovolt. Res. Appl. **21**(3), 308–318 (2013).
9. S. Askins, M. Victoria, R. Herrero, and C. Domínguez, "Optimizing CPV systems for thermal and spectral tolerance," in *Proc. 27th EU PVSEC* (2012), pp. 194–198.
10. P. Benítez, J. C. Miñano, P. Zamora, R. Mohedano, A. Cvetkovic, M. Buljan, J. Chaves, and M. Hernández, "High performance Fresnel-based photovoltaic concentrator," Opt. Express **18**(1), A25–A40 (2010).
11. I. Antón, C. Dominguez, M. Victoria, R. Herrero, S. Askins, and G. Sala, "Characterization capabilities of solar simulators for concentrator photovoltaic modules," Jpn. J. Appl. Phys. **51**(10S), 1–4 (2012).
12. C. Domínguez, I. Antón, G. Sala, and S. Askins, "Current-matching estimation for multijunction cells within a CPV module by means of component cells," Prog. Photovolt. Res. Appl. **21**(7), 1478–1488 (2013).
13. W. Smith, *Modern Optical Engineering; The Design of Optical Systems, 3rd Edition* (McGraw-Hill, 2000).
14. H. P. Baltes, *Inverse Scattering Problems in Optics* (Springer-Verlag Berlin Heidelberg, 1980).
15. M. Victoria, "SOE for Fresnel lenses," in *New Concepts and Techniques for the Development of High-Efficiency Concentrating Photovoltaic Modules* (Academic, Universidad politecnica de Madrid, 2014), pp. 48–49.
16. T. Hornung, M. Steiner, and P. Nitz, "Estimation of the influence of Fresnel lens temperature on energy generation of a concentrator photovoltaic system," Sol. Energy Mater. Sol. Cells **99**, 333–338 (2012).
17. T. Hornung, A. Bachmaier, P. Nitz, A. Gombert, A. W. Bett, R. D. McConnell, G. Sala, and F. Dimroth, "Temperature dependent measurement and simulation of Fresnel lenses for concentrating photovoltaics," in *CPV6 Conf. Proc.* (Amer Inst Physics, 2010), pp. 85–89.
18. R. Mohedano, P. Benitez, P. Zamora, J. C. Miñano, J. Mendes, A. Cvetkovic, J. Vilaplana, M. Hernandez, J. Chaves, and G. Biot, "Ventana power train features and performance," in *CPV9 AIP Conf. Proc.* (Amer. Inst. Physics, 2013), pp. 176–179.
19. I. Garcia, P. Espinet-Gonzalez, I. Rey-Stolle, E. Barrigon, C. Algora, F. Dimroth, S. Kurtz, G. Sala, and A. W. Bett, "Extended triple-junction solar cell 3d distributed model: application to chromatic aberration-related losses," in *CPV7 Conf. Proc.* (Amer. Inst. Physics, 2011), pp. 13–16.

---

1. Introduction

A multi-junction solar cell (MJSC) is a series-interconnected stack of semiconductors where each harvests a different band of the solar spectrum to more efficiently transform sunlight into electricity. Concentrator photovoltaics (CPV) systems then leverage inexpensive optical components to concentrate light onto these highly efficient small area cells. World record cell and module efficiencies of 46% and 38.9%, respectively [1, 2], have been achieved using MJSCs under concentration. With the increase in global cumulative deployment volume and a consistent decrease in system cost, CPV systems now cost as little as 1 $/W, and the costs continue to fall faster than for traditional photovoltaics systems [3]. However, the necessary use of concentrating optics may result in chromatic aberration and a nonuniform illumination profile across the MJSC, thus reducing its electrical performance. Spatial non-uniformity increases the losses due to cell series resistance [4,5]. Spectral inhomogeneities will increase losses due to local subcell current limitations [6]. The inhomogeneity of irradiance and spectrum are given by the optical design, but these properties are highly sensitive to other factors like the distance between the primary optical element (POE) and the receiver, the POE temperature [7, 8], or the presence of a secondary optical element (SOE) [9]. Thus, these factors can be used to tune the inhomogeneity of intensity and spectrum.

An indoor optical-electrical measurement methodology has been developed to characterize the spatial and spectral nonuniformity produced by CPV optics. CCD or CMOS image sensors are commonly used to measure the light intensity distribution cast by the optics in a CPV system [6]. The current generation profile of a cell can be studied through images taken at different wavelengths and, in conjunction with electrical measurements, allows in depth analysis of single-lens module behavior under various conditions. We first present the test bench instrumentation and the calibration procedures for spectral imaging. Next, the top and middle subcell currents are calculated from the spectrally resolved images and compared to their isotype meaurements. Finally, the impact of primary lens temperature is demonstrated by comparing the opto-electrical performance of two systems: (1) a silicone on glass Fresnel lens without a secondary; and (2) a PMMA, four Fresnel-Köhler (4FK) lobe system [10].

#251636 Received 15 Oct 2015; revised 20 Nov 2015; accepted 22 Nov 2015; published 7 Jan 2016

2. Experimental setup

The METHOD testbench, shown schematically in Fig. 1, allows both optical and electrical characterization of CPV systems. This experimental technique is realized with a HELIOS solar flash simulator, an indoor solar simulator that produces direct normal irradiance on a CPV system and uses reference sensors to monitor both the spectrum and concentration through a 2 ms flash from a xenon bulb [11]. The light is collimated using a 2 meters diameter parabolic mirror on the testbench. It is comprised of an *imaging module*, an *electrical module*, and a *reference measurements* section. A thermal chamber encloses the POE with solar glass on both the front and rear surfaces, allowing light to pass through, which decouples the temperature of lens and cell. It is mounted on a positioning stage that can be moved to cast the light from the POE either on the imaging module or the electrical module. The POE can be heated from 25°C to 60°C by two compact heaters installed on either side of the thermal chamber. The thermal uniformity of the POE is ± 1C° under cooling at a rate of 1C°/minute.

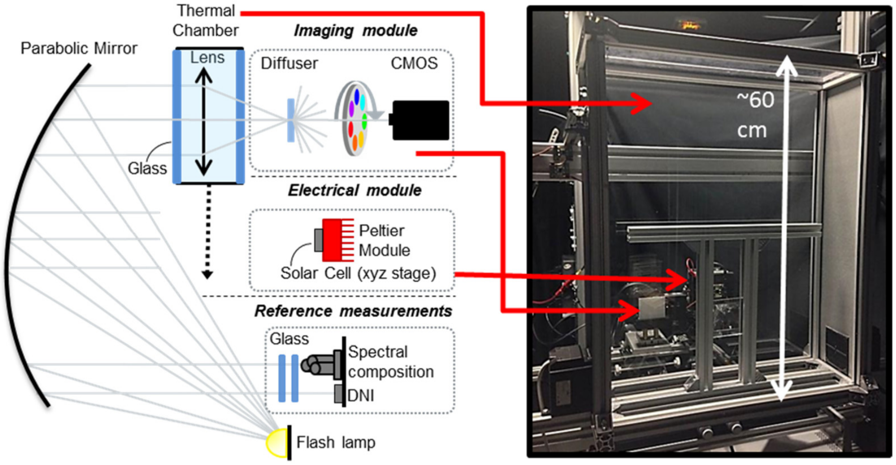

Fig. 1. Schematic of the instrumentation used in the METHOD testbench.

The *imaging module* consists of an opal diffuser, a filter wheel with twelve 50 nm (full width half maximum) bandpass filters, and a near infrared (NIR) CMOS camera. This type of sensor allows acquiring signal for the spectral region 350-1100nm. The collimated beam from the xenon flash is focused by the POE onto the diffuser located at the focal plane of the camera. This location corresponds to the position of the MJSC under electrical measurement. A diffuser is used since its near-Lambertian response allows a common focal plane to be established for all spectral ranges, while capturing the full chromatic aberration of the POE. An opal diffuser was selected since it has a better lambertian behavior in the visible spectrum over a typical ground glass diffuser. The filters were selected to divide the intensity profile into twelve separate spectral bands in order to fully characterize top and middle subcells and to fit the 350 to 1100 nm spectral response of the camera. The central wavelengths of the filters range from 400 nm to 950 nm, in 50 nm increments. The camera captures a 12.8 x 10 mm image with a resolution of 1280 x 1024 pixels (1 pixel = 10 μm^2). In order to capture the image at the correct time within a pulse, an external photodetector is used to trigger the camera. The output of the Imaging System is a set of 12 images, acquired within 20 seconds.

Spectral respone of the camera and filters limits the *imaging module* to only study the top and middle subcells of a triple-junction cell. This has a limited impact for conventional CPV module, using lattice-matched triple-junction cells. However, bottom subcell of such device are known to produce an excess of photogenerated current under outdoor conditions. Therefore, the top and middle subcells will limit the total photogenerated current since the subcells are connected in series. Moreover, dispersion of CPV optical materials is relatively low for wavelengths above 1100nm, and light distribution seen by the bottom subcell is similar to the middle subcell. Results presented in this work are therefore considered for top and middle subcells.

The *electrical module* consists of a MJSC mounted on a Peltier module to maintain a stable cell temperature from 20°C to 100°C with 0.1°C precision. The Peltier module is fixed on an *x-y-z* translation stage to optimize or vary the cell position with respect to the POE. Since the incident spectrum varies across the temporal profile of the flash (and from flash to flash) due to changing lamp temperature, the spectral composition of the incident light is measured by individual subcell isotypes [11, 12]. To link the measurements of the reference instruments and the device under test, it is sufficienty to place two panels of the same glass that encloses the thermal chamber in front of the reference measurement instruments. This allows the METHOD testbench to be used to study the effects of POE temperature, or cell position, on the electrical performance and irradiance profile of a given CPV system.

3. Spectral irradiance profile measurement technique

Here we discuss how raw images from the Imaging System are converted into spectral band irradiance profiles and how the generated currents of top and middle subcells are obtained. The calibration procedure to obtain a spectrally resolved irradiance distribution is first described, then its validation with electrical measurements.

3.1. Calibration procedure to obtain the spectrally resolved irradiance distribution

In order to quantify the spatial dependence of each 50 nm spectral irradiance band across the MJSC, the CMOS camera images must be calibrated. There are four calibration factors that must be applied to the CMOS signal to transform pixel counts to a final irradiance value. Each filter and pixel are represented by index *i* and coordinate system x,y, respectively. A dark image is taken to account for thermal noise, which is subtracted from the raw image measured under illumination. The resulting signal $S_i(x,y)$ is then calibrated to produce a spectral irradiance $F_i(x,y)$, in W/m^2/nm, as

$$F_i(x,y) = S_i(x,y) \Big/ C_i^{tot}(x,y) \tag{1}$$

where

$$C_i^{tot}(\mathrm{x,y}) = C_i^{pow} \cdot C_i^{unif}(\mathrm{x,y}) \cdot C_i^{lin} \cdot C_i^{adj} \tag{2}$$

is the total calibration factor comprised of C_i^{pow}, which addresses the conversion from counts to W/m^2/nm; $C_i^{unif}(x,y)$, which accounts for any spatially non-uniform response across the image sensor; C_i^{lin}, which corrects for nonlinearity in camera response; and C_i^{adj}, which adjusts for the actual filter response.

The first factor to apply, C_i^{pow}, converts pixel counts to irradiance values. The total irradiance seen by the camera was determined by placing a calibrated source a fixed distance from the diffuser and integrating its known spectrum with the known filter transmittance for each filter. Since diffuser transmission depends on incident angle, this calibration was done over all relevant angles and an appropriate average then detemined. Figure 2 shows the extracted calibration constants for each filter, denoted by its central wavelength, at six angles ranging from normal incidence to 25°, shown sequentially by the color-coded bar graph. In

#251636 Received 15 Oct 2015; revised 20 Nov 2015; accepted 22 Nov 2015; published 7 Jan 2016

reference to the dark blue bars (normal incidence) in Fig. 2, the calibration constant of the filters with a central wavelengths above 700 nm begin to diverge from the off-axis results as the lambertian behavior of the diffuser increasingly breaks down due to increased forward scattering [13,14]. Therefore, the forward scattered light in this frequency range will result in a misrepresentative sensor reading and a false calibration factor. Nevertheless this effect can be observed for a limited number of ray angles, as observed on Fig. 2, and we will neglect the forward scattered component at long wavelengths in our approach. The remainder of the data show variations on the order of 10%, which implies that any final calibration factor will not be sensitive to the angular averaging procedure. For convenience, we chose to use the 15° results as representative of average calibration factors since this is close to the median angle of typical Fresnel concentrators under consideration [15].

The second factor, $C_i^{unif}(x,y)$, accounts for any spatially non-uniform response across the image sensor. Ideally, the camera's digital response from each pixel will be the same for a given illumination, but in practice the response across the image sensor varys by about 5%. To determine the correction factor for each pixel, uniform illumination on the diffuser across the camera's field of view was achieved with a calibration lamp. The correction factor for each pixel was determined by dividing each pixel by the mean of the image.

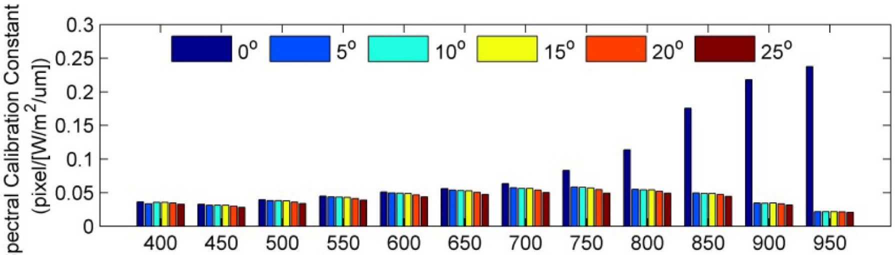

Fig. 2. Dependence of the spectral calibration constant on incident angle to the diffuser for each filter.

The third correction factor, C_i^{lin}, accounts for any non-linear response of the electronics to variations in light intensity. Ideally, the response of the sensor would be a signal directly proportional to the light incident on each pixel, but the electronics introduce a slight nonlinear response, up to 2%, particularly near the noise floor and near saturation. Therefore, characterizing the linearity of the signal for each filter has been calculated with a calibrated lamp, varying the intensity at the sensor through adjusting the integration times of the camera.

The final correction factor, C_i^{adj}, accounts for non-ideal filter response and any spectral overlap, since the initial presumption is 100% transmission over contiguous filter bins. The final goal is to reproduce spectral irradiance on the diffuser for spectral band of 50 nm. However, the transmittance of the filters is not 100% over their full range and the result is a non-perfect rectangular transmission of light and a slight overlaps between bands. Therefore, a simple correction is applied to account for this phenomenon: for a Xenon lamp spectrum equivalent to the spectrum AM1.5D, the transmitted light power ratio between ideal and real filters are calculated. These values are then applied as correction factors.

The spectrally resolved irradiance distirbution seen by a MJSC in a CPV system can now be calculated from the images acquired through the *imaging module*. In Fig. 3, the 2-dimensional cross section plot of the corrected irradiance profiles for a silicone on glass POE can be viewed for a 5x5 mm^2 area on the diffuser. The cross-section is taken for a central line of the spot. All twelve images are acquired at a fixed diffuser to POE distance. For clarity, only selected wavelengths are plotted since there is little difference in profiles at higher

#251636 Received 15 Oct 2015; revised 20 Nov 2015; accepted 22 Nov 2015; published 7 Jan 2016

wavelenghts. The profiles illustrate the wavelength dependence due to chromatic aberration of the POE. This phenomenon can be seen when comparing the profiles at 950 nm to 400 nm, where the longer wavelengths are more tightly focused than the lower wavelengths. The asymmetry of the profiles can be related to the imaging properties of the POE. Since the source is a xenon bulb and not a uniform light source, its shape is imaged onto the diffuser.

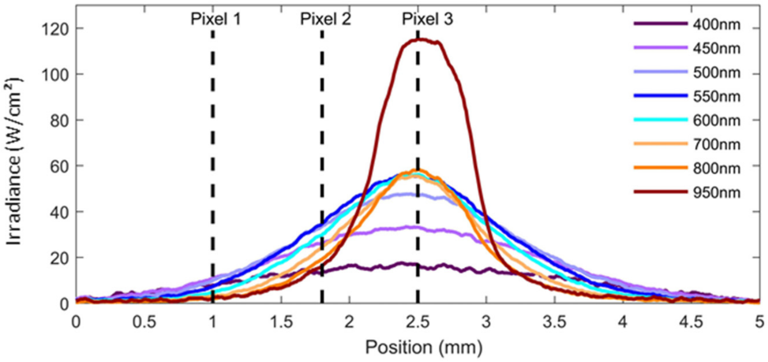

Fig. 3. Cross-sections of the intensity profile for transmission through each filter.

The irradiance values calculated in Fig. 3 are used to generate a spectrum of 50 nm resolution for each pixel (25M points on the 5 x 5 mm^2 area). To illustrate this, the spectral irradiance of three separate pixels showing a different spectral balance due to the chromatic aberration on the diffuser, or as seen by a MJSC, are represented in Fig. 4. The pixels are chosen on the edge of the beam profile. The spectra are normalized by their power to better compare their spectral composition. Due to chromatic aberration, at the edge of the profile (pixel 1), the spectrum is strongly blue shifted. As we move toward the centre of the beam, the spectrum becomes more balanced (pixel 2), and at the beam centre (pixel 3), the spectrum becomes red-rich.

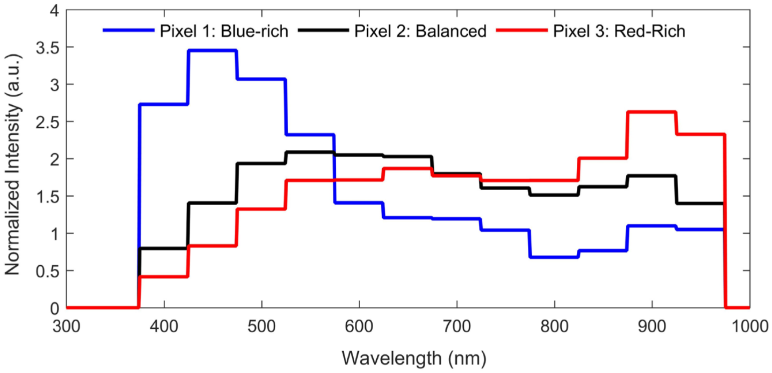

Fig. 4. Spectral irradiance is represented for 3 positions of the cross-section in Fig. 3. The spectra are normalized to their power under concentration for better comparison.

3.2 Validation of spectral irradiance calculation with electrical measurements

The local subcell current densities, $J_i(x,y)$, of a solar cell can be calculated from the spectrally resolved irradiance obtained by the imaging process as,

$$J_i(x,y)=\sum_{\lambda}\frac{q\lambda}{hc}.e(\lambda,x,y).EQE_i(\lambda) \tag{3}$$

where EQE_i is the measured external quantum efficiency for each subcell i and $e(\lambda,y,z)$ is the local irradiance at each point density: Then, the short-circuit currents, $I_{sc,i}$, for each subcell can be calculated from the following equation:

$$I_{sc,i}=\sum_{x,y}J_i(x,y).A_{pixel} \tag{4}$$

where A_{pixel} corresponds to the pixel area and x, y are the position on the cell constrained by the total surface area of the cell. We now compare currents calculated from the image profiles to those measured by the top and middle subcell isotypes (5x5 mm^2) of a lattice matched MJSC from Spectrolab. The POE used in this study is a SOG Fresnel lens designed for concentrating the light 500X on a 3 mm diameter cell.

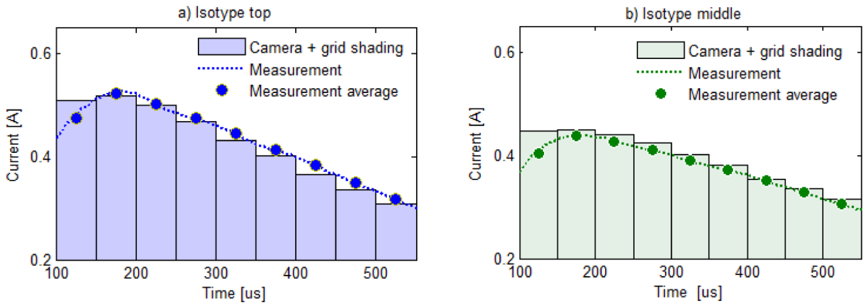

Fig. 5. Comparison of photogenerated currents determined by the mean of spot imaging and from electrical measurements of top (a) and middle isotypes (b). Measure average corresponds to an average on a 50 μs period, equivalent to the integration time used for image acquisition.

The measured short circuit currents of the isotypes are compared to the currents calculated from the spectral images for a given flash, and the data presented in Fig. 5. The integration time of the camera was set to 50 μs and images were captured at different points along the flash. Adding in known grid shading losses of 5%,, we obtain an underestimation of 3% and an overestimation of 2% for the top and middle subcell, respectively. From these results, the forward scattered light of the diffuser for wavelengths greater than 700nm did not introduce a significant increase of calculated middle subcell current. When accounting for the non-flat filter response, angular distribution of incident angles, and diffuser-related issues described, these results are satisfying for the conversion methodology and the lens tested. For other optical concentrators, comparing current measured and calculated can be considered a necessary validation process.

4. Results

In order to illustrate the capabilities of the METHOD test bench, we will first study a SOG lens with a 376X geometrical concentration factor in combination with a 10 x 10 mm^2 Emcore triple-junction cell. The focal distance given by the manufacturer is 285 mm, and there is no SOE.

The first test performed was to generate different spot profiles depending on lens temperatures. Results are presented in Fig. 6 for four temperatures. Current densities are given for a cell I_{SC} corresponding to STC conditions (1000 W/m^2), *i.e.,* 4.2 A at $T_{\text{lens}} = 20°\text{C}$. For the sake of simplicity and a better representation of current density evolution with lens temperature, this I_{SC} value is used for calculating current densities at other lens temperatures.

First, there is an asymmetry in the current density plots. This shape appears because the SOG lens is imaging the toroidal shape of the xenon lamp.The shape is visible depending on spectral range due to the wavelength dependence of the focal distance. However even though its spot shape differs from on-sun conditions, comparable chromatic aberration exists and the spectral non-uniformities caused by the POE on the MJSC can be observed.

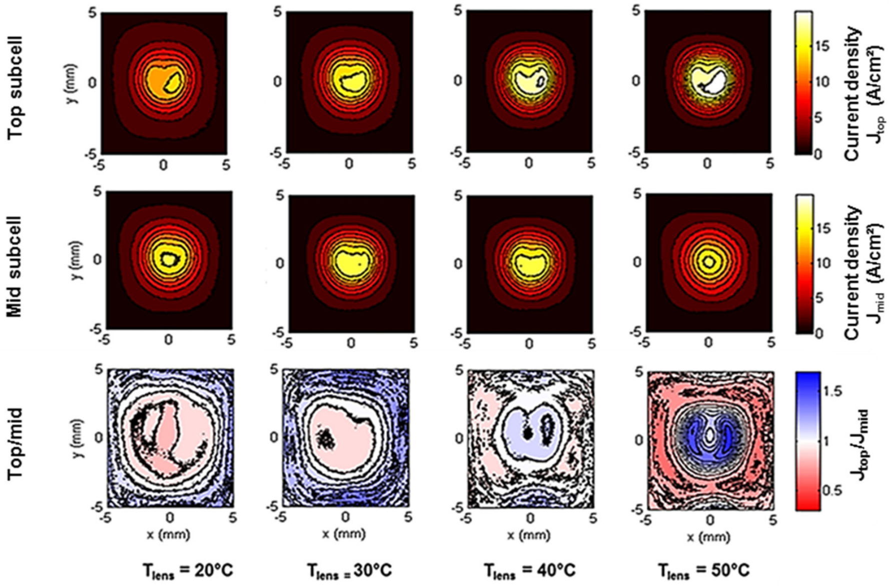

Fig. 6. Top and middle subcells current densities determined with the imaging system, and the resulting J_{top}/J_{mid} ratio showing its dependence on lens temperature for a 376 cm^2 SOG lens focusing light on a 1 cm^2 area. For helping comparisons, J_{sc} values at elevated temperatures are based on normalised values of the current I_{sc} at standard temperature conditions.

Now, we consider the evolution of current densities J_{top} and J_{middle} with POE lens temperature. Values of maximum current densities for both subcells are between 12 and 18 A/cm^2, depending on lens temperature. These values correspond to a peak to average ratio (PAR) between 2.9 and 4.3, respectively. As the POE temperature increases, the PAR of the top subcell current density profile also increases, creating a higher amount of current in the center of the cell. The middle subcell current density, however, remains stable. Due to these different trends, at T_{lens} = 20°C the spatial current density from the top differs only slightly from that of the middle, whereas at T_{lens} = 50°C, the difference is striking. The physical mechanism responsible of the temperature dependence of Fresnel lens is explained in [16,17], and is related to thermal expansion of the optic material. Thermal expansion causes a decrease in the refractive index of the lens, resulting in an increase in focal length. Moreover, the shape of the Fresnel facets is modified leading to a beam shape distortion.

The beam distortion and chromatic aberration is quantified by the temperature evolution of the top to middle subcell current ratio. The observed ratio ranges from 0.85 to 1.15 and from 0.5 to 1.5, for T_{lens} of 20°C and 50°C, respectively. At higher POE temperatures, there is a higher spectral mismatch between the top and middle subcells. Furthermore, there is a difference in the spatial current limitation. In reference to Fig. 6, at T_{lens} = 20°C, the light focused at the center of the cell corresponds to a red-rich spectrum, demonstrating a top subcell current limiting zone. As the temperature is increased, the center of the cell becomes middle-limited due to a blue-rich spectrum. Consequently, this phenomenon has an impact on the global current matching of the cell. At T_{lens} of 20°C and 50°C, the observed global $J_{\mathrm{top}}/J_{\mathrm{mid}}$ ratios are 0.98 and 1.04, respectively. The primary-to-cell distance set by the manufacturer is well adapted for lab conditions for a spectrum equivalent to AM1.5D (SMR = 1) and lens temperature equal to 20°C. However, it is evident that, once the system is subject to changes in POE temperature or incident spectrum, there is a significant impact on performance. In the field, lens temperature and spectrum will vary throughout the day. The optimal cell position may therefore be different than the one determined under STC conditions.

We now compare two fundamentally different devices with respect to lens temperature. Device A is a SOG lens concentrator (~500X) focusing light on a 7 mm^2 Azurspace cell with a circular shape. The POE-cell distance was set to 96mm from the POE, corresponding to an optimized power production at a lens temperature of 25°C. Device B is a PMMA 4FK lobe concentrator [18] corresponding to a fourfold two-stage optical concentrator. It combines a Fresnel lens POE and a refractive SOE, splitting the light into four Köhler channels. The POE-cell distance set by the manufacturer is 260 mm. The geometrical concentration is ~1000 X, defined over 5 x 5 mm^2 illuminated Emcore cell. The *I-V* curves shown in Fig. 7 where taken at 600 W/m^2 with a blue blue-rich spectrum corresponding to an SMR value of 1.1.

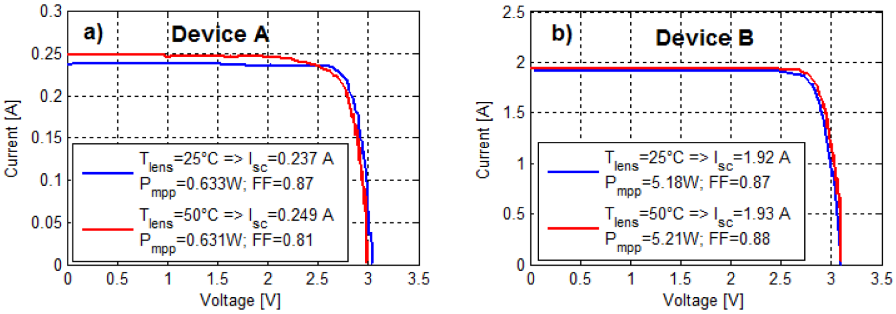

Fig. 7. *I-V* curves of two different concentrator technologies for two lens temperatures. (a) Device A is a single optical element concentrator (SOG lens); and (b) Device B is a 2 stage Fresnel-Köhler concentrator.

Figure 7 shows a difference in electrical performance depending on lens temperature for device A. However, the temperature of the POE minimally affects device B. More specifically, device A has an increase of 5% in the short circuit current at high lens temperature. However, there is a drop in fill factor of 0.87 to 0.81. The variation in terms of efficiency is therefore not significant in this case, and both systems show similar performance in terms of power produced when lens temperature is increased.

To study device behavior, we have performed spot imaging analysis for two extreme lens temperatures. Trigger delay for image acquisition is set up so that *I-V* curve measurement is taken at the same point in the flash. As mentioned in section 3, electrical measurements are used to scale current densities determined with the *imaging module* to the I_{sc} measured on the *I-V* curve. Figure 8 illustrates two parameters of interest: the $J_{\mathrm{top}}/J_{\mathrm{mid}}$ ratio, and a cross-section of the current density generated by top and middle subcells, normalized by the mean current density for the cell size considered. A cross-section is taken for a central line of the spot. Our first observation concerns the spatial distribution of light intensity. Device A gives a spot with a gaussian profile whereas device B produces a spot with a much more uniform distribution. The absence of an SOE in the case of device A explains such optical behavior, whereas the 4FK optic is known to produce a highly uniform pattern [10,18]. This non-uniformity can be quantified through the maximum value of the normalized current density plot. We will consider this value to be the PAR for the spot. The top subcell PAR values for device A are 3 and 4, for T_{lens} of 25°C and 50°C, respectively. However, device B presents a flat normalized current density of 1.2 for a central area of 4 x 4 mm^2 side.

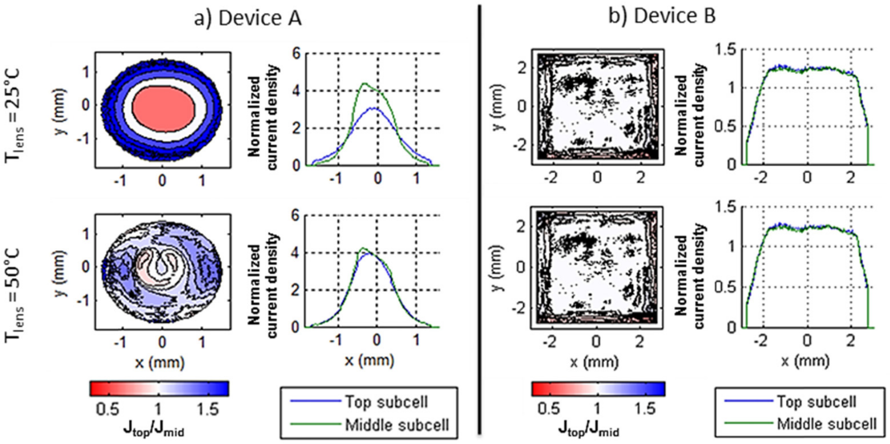

Fig. 8. $J_{\mathrm{top}}/J_{\mathrm{mid}}$ ratio and the current density normlized by the average value on the cell for a centered cross-section of the spot for 2 different concentrators, (a) Device A, and (b) Device B.

In the case of device A, notable chromatic aberration can be observed. At T_{lens} = 25°C, a red-rich spectrum is focused at the center of the cell, whereas on the edges, the light is blue-rich. The result is a global $J_{\mathrm{top}}/J_{\mathrm{mid}}$ ratio of 0.92. The normalized current density profiles for the top and middle subcell introduce strong spatial current limitation forcing lateral current flows within the device [19]. For T_{lens} = 50°C, the PAR of the top subcell increases and there is greater balance in the current generation profiles resulting in a global current matching of 0.97. Furthermore, there is a decrease in lateral current flows. The effects that this has on system electrical performance are seen in Fig. 7. At T_{lens} = 50°C, there is an increase in short circuit current due to higher degree of over all current matching between the subcells. Furthermore, with a lower PAR of the limiting subcell at a T_{lens} = 25°C, the fill factor will be higher. The drop in fill factor at higher temperature can be explained by the increase in PAR. As the PAR increases, there will be more current generated in the middle of the subcell resulting in higher series resistance.

In agreement with electrical measurements, the optical behavior of device B is tolerant to changes in POE temperature. Altough less sensitive to temperature (compared to SOG), PMMA's index of refraction still changes with temperature, and so alters the focal distance and spot profile. This change is not significant enough to induce a visible change at the output of the 4FK secondary optic. The POE-SOE combination of device B therefore balances the thermal sensitivity of the POE against chromatic mismatch produced by concentrator misalignments, as shown in [9].

5. Conclusions

A test bench, METHOD, has been presented along with a methodology for measuring the spectrally resolved irradiance distribution of a CPV optical system. The spectral imaging process can be applied to different CPV systems to create current generation profiles to analyze CPV system performance as a function of POE lens temperature. The indoor test bench allows for full independent control of POE and cell temperatures in order to study the CPV performance under the various conditions it will face in the field. Comparing these profiles to electrical measurements of the system under the same conditions can provide

#251636 Received 15 Oct 2015; revised 20 Nov 2015; accepted 22 Nov 2015; published 7 Jan 2016

greater insight into the effect of non-uniform illumination profiles and chromatic aberrations on the cell electrical performance.

Acknowledgments

The author thanks LPI and Soitec for their collaboration and all other partners involved. Partial funding from the European Union's Horizon 2020 research and innovation program within the project CPVMatch under grant agreement No 640873, and Natural Science and Engineering Research Council of Canada (NSERC), are acknowledged. The authors are solely responsible for the content of this work and it only reflects the author's view. The European Commission or any of their agencies are not responsible for any use that may be made of the information it contains.

Chapter 4

Detailed study of irradiance profile and chromatic aberrations in CPV optics

4.1 Effects of Lens Temperature on Irradiance Profile and Chromatic Aberration for CPV Optics

4.1.1 Scope and contribution

This publication explains the value of the test-bench, discussed in the previous chapter, to quantify the effects of lens temperature on the spatial and spectral non-uniformities of refractive optics in CPV systems. When operating at a different temperature, the irradiance profile at the surface of the individual subcell can drastically change, affecting the performance of the system.

This was the first time that such an in-depth analysis was performed on three specific commercial optical architectures, which included a SoG Fresnel primary without a secondary optic, a PMMA Fresnel primary with a glass truncated inverted pyramid, and a 4 Fresnel-Köhler design. The analysis described in the following publication shows that there is a temperature dependence for all three commercial modules and constitute preliminary results that demonstrate how important lens temperature can be in relation to the performance of a CPV system and annual energy yield calculations, which will be discussed further in Chapter 5. The measurements were taken at CAE-INES in France with Dr. Besson. All the post processing analysis and writing were done in Ottawa by the first author with editing help from the coauthors.

4.1.2 Publication

Patrick McVey White, Pierre Besson, Mathieu Baudrit, Henry Schriemer, and Karin Hinzer, “Effects of lens temperature on irradiance profile and chromatic aberration for CPV optics,” *CPV-12*, Freiburg, Germany, AIP Conference Proceedings **1766**, 040004 (2016).

Paper attached on the next page.

Effects of Lens Temperature on Irradiance Profile and Chromatic Aberration for CPV Optics

Patrick McVey-White[1], Pierre Besson[2], Mathieu Baudrit[2], Henry P. Schriemer[1], and Karin Hinzer[1]

[1] *SUNLAB, Centre for Research in Photonics, University of Ottawa, Ottawa, Ontario, Canada*
[2] *CEA-LITEN, INES, Le Bourget du Lac, France*

Abstract. Lens-based optical concentrators are currently the most common in concentrator photovoltaic systems. This paper discusses experimental results to quantify the effects of temperature on the primary optical elements of three commercial Fresnel-based designs. The designs are: Silicon on Glass Primary with no secondary, PMMA Primary with a Truncated Inverted Pyramid secondary, and a PMMA 4 quadrant Fresnel – Köhler system. We quantify the effects of temperature on the irradiance profile with the variation in peak to average ratio of from 25 – 50 ° C. Furthermore, the effect of temperature on chromatic aberration is represented with the ratio of the top subcell current to middle subcell for a standard triple junction germanium-based cell. For the system with the lowest peak-to-average ratio, PMMA-based 4 Fresnel-Kohler design, we observed a change of 2% in the subcell ratio when the lens was heated to 50 ° C.

INTRODUCTION

Concentrator Photovoltaics (CPV) can concentrate light by means of refraction onto high-efficient multi-junction solar cells (MJSC) to reduce the amount of MJSC surface area. However, due to the dispersion within the material of the primary, non-uniform illumination patterns and chromatic aberrations are introduced. Additionally, the materials used to manufacture these primaries are sensitive to temperature and humidity [1]. This is important since CPV systems are subject to a large range of ambient temperatures in the field. Therefore, their performance is adversely affected due to the temperature dependence of the optical and electrical components. The latter has been studied extensively in the literature, the shift in semiconductor bandgap energies towards higher wavelengths, which can be calculated with the Varshni model, does not have a significant impact on the system performance and annual energy yield [2, 3, 4]. By contrast, the impact of optical temperature on optical performance continues to be a subject of discussion since it has a direct effect on the total energy harvested [5, 6]. A recent study on various optical concentrators has shown, how cell to lens distance affect non uniformities, hence module performance [7]. As a consequence, there is greater mismatch between local subcell current densities, leading to depression of the fill factor and thus reduced system efficiency [5, 7]. In this work, we use a technique to spectrally image the irradiance profiles of three CPV systems to determine the influence that temperature has on chromatic aberration, current generation, and thus the overall module performance.

OPTICAL IMAGING OF CPV SYSTEMS

CPV systems with Fresnel-based POEs have shown a temperature dependence on optical performance that adversely affects system performance [8, 9]. Specifically, increasing temperature drives thermal expansion of the primary material and decreases its refractive index, increasing the focal length and change in the shape of the lens. This results in a change in the intensity and spectral profiles across the MJSC. To better understand the system response, the temperature dependence of these profiles must be determined to study how each individual systems deals with the temperature sensitivity of the primary. This study looks into the temperature effects for three systems: a Silicone on Glass (SoG) Fresnel POE without a Secondary Optical Element (SOE), a polymethylmethacrylate (PMMA) Fresnel POE with a Truncated-Inverted-Pyramid (TIP) SOE, and a four quadrant PMMA Fresnel primary and BK7 Köhler secondary (4-FK) system with fourfold two-stage concentrator design, shown respectively in Figure 1 below.

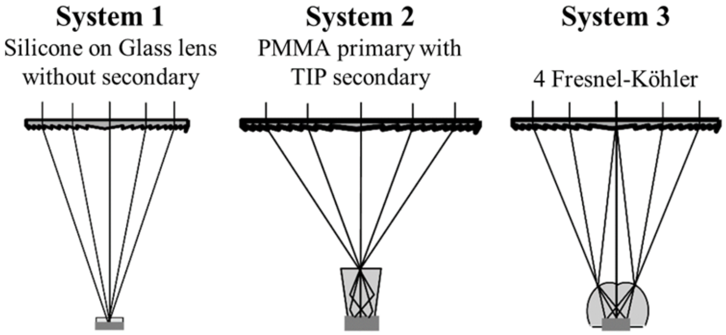

FIGURE 1. System 1: SoG Fresnel POE without A secondary; System 2: PMMA Fresnel POE with a TIP secondary; and System 3: 4-FK [12].

In order to isolate the impact that the temperature has on optical system performance, the temperature of the POE must be adjusted while maintaining the other elements in the optical train fixed. We have achieved this with the Automated Controlled Thermal Tech-bench (ACTT), which consists of a thermal chamber and an optical imaging system [8]. The thermal chamber is a thermal-controlled glass enclosure that houses the primary. Light enters at normal incidence and is then focused through the rear glass, across a range of angles, onto the SOE (or the surface of the MJSC) – see Fig. 1. We adjust for Fresnel reflection losses at all interfaces. The imaging system of the CPV-ACTT captures the spectral profile from 350 to 1000 nm with 50 nm resolution via a CMOS detector coupled with twelve bandpass filters. In order to provide an equivalent image plane, the MJSC was replaced by a diffuser, and the SOE glued to it using silicone. The diffuser configurations for the three systems can be seen in Fig. 2. The methodologies and characterization of the CPV-ACTT can be found in [8].

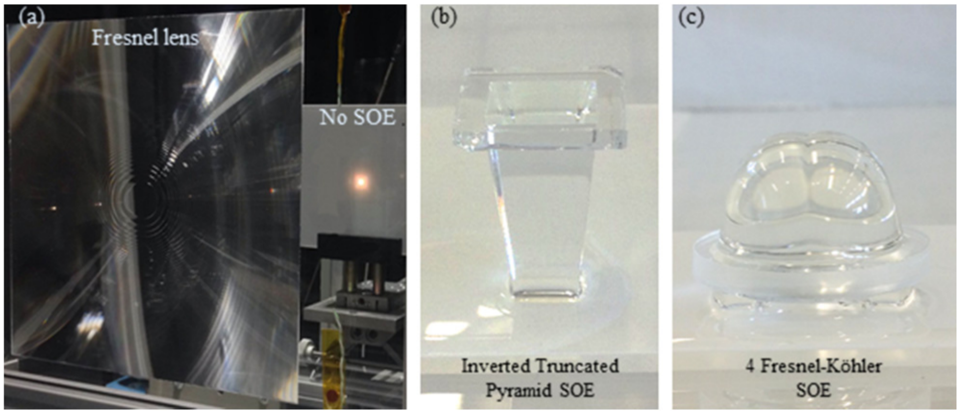

FIGURE 2. The diffuser set-up used to optically image the temperature effects on chromatic aberration for (a) SoG Fresnel lens POE focusing without an SOE, (b) Fresnel POE and an TIP SOE and (c) the 4 Fresnel POE with the Kohler SOE.

LENS TEMPERATURE EFFECTS ON IRRADIANCE PROFILE

CPV systems typically employ Fresnel lenses as primary concentrating elements, where the large area of inexpensive optics offsets an expensive MJSC footprint. The essentially planar character of the Fresnel lens, enabled by the serrated face, in conjunction with a SOE permits wide acceptance angles for concentration ratios that can exceed 500 suns (1 sun = 1,000 W/m^2). However, Fresnel lenses still produce non-uniform irradiance profiles, and SOEs are used in an attempt to flatten them. When incident on a MJSC, nonuniform profiles cause gradients in the local current density, which lead to resistive losses, and so directly impact system performance [5]. This section will reveal the temperature dependence of the irradiance profiles for the three systems.

The design of a CPV system can be optimized to address the ohmic losses arising from a nonuniform irradiance profile. Since design are typically done under standard test conditions, a fixed temperature irradiance profile is used to set the cell to POE distance. However, the lens experiences a range of temperatures when deployed under field conditions, and the pattern incident on the MJSC may change due to the change refractive index and geometry of the lens with temperature [10]. Therefore, the efficiency of the system may no longer be optimal since the optimization conditions have changed. Fig. 3 shows the measured irradiance profile of System 1 as the primary is heated from 25° ^{C} to 50° ^{C}. It is evident that there is a high degree of temperature dependence. In reference to Fig. 3, there is a slight increase in peak irradiance and an increase of 12.4% in total irradiance at 30° ^{C}. Furthermore, past 30° ^{C} the performance of the optic decrease as it drops a total of 81.2% at 50° ^{C}, which can affect the performance of the MJSC. The performance of the primary shows how temperature will affect the focal distance.

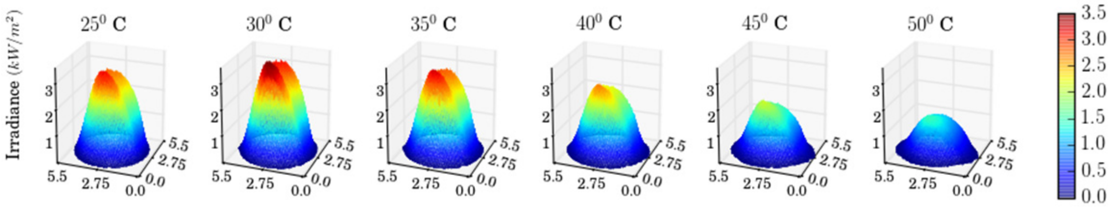

FIGURE 3. Measured irradiance profile of a SoG Fresnel POE with no SOE at a POE temperature of 25$^{\circ\, C}$ to 50$^{\circ\, C}$.

An SOE aids in confining the irradiance profile to the cell face while enhancing uniformity. System 2 has a TIP kaleidoscope SOE, which exploits total internal reflection to achieve better uniformity at its exit aperture when the number of reflections exceeds one [11]. The global edge-rays of the POE are used to optimize the entry size and height of the SOE to ensure an optimal number of reflections under the design conditions. Fig. 4 shows the evolution of the irradiance distribution for System 2 when its POE heated is from 25$^{\circ\, C}$ to 50$^{\circ\, C}$. Compared to the System 1 scenario at 25$^{\circ\, C}$, the uniformity across the MJSC is drastically improved. Moreover, the profiles remains fairly stable up to 40$^{\circ\, C}$ then there is a slight increase in irradiance and a drop in uniformity as the temperature further increases. This is because the focal distance is no longer optimized to the SOE entry aperture, so the number of internal reflections of the incident rays decreases and the peak-to-average-ratio (PAR) increases. The result, an increase of 8.5% in total irradiance compared to 25$^{\circ\, C}$. The deleterious impact on CPV module efficiency that this produces has been noted [12].

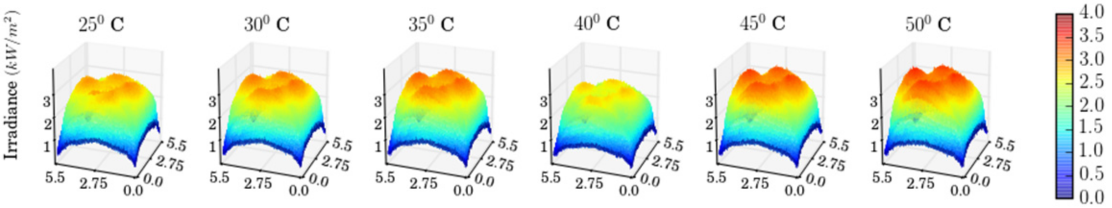

FIGURE 4. Measured irradiance profile of a Fresnel POE with inverted pyramid SOE at a temperature of 25$^{\circ\, C}$ to 50$^{\circ\, C}$.

SOEs can be a markedly improved if Köhler integration techniques are exploited to design SOE response in conjunction with POE design. System 3 is a 4-FK system, where the four-fold symmetries of both POE and SOE are arranged such that rays focused by one quadrant of the POE onto the corresponding SOE segment are then refracted across the cell face. Fig. 5 shows the largely unchanging character of the essentially flat irradiance distribution for System 3 when it's POE heated is from $25^{\circ\,C}$ to $50^{\circ\,C}$, demonstrating the superiority of the 4-FK design with a 2% increase in total irradiance.

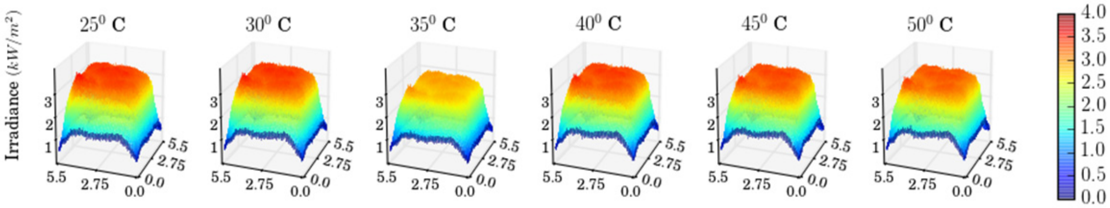

FIGURE 5. Measured irradiance profiles of a 4-FK at POE temperatures from $25^{\circ\,C}$ to $50^{\circ\,C}$.

LENS TEMPERATURE EFFECTS ON CHROMATIC ABERRATION

The irradiance profiles shown above correspond to the broadband spectral distribution across the MJSC. The subcells of the MJSC, however, harvest spectrally distinct bands as determined by their quantum efficiencies. Differences in the irradiance distributions can also occur between subcells. These differences, which may be referred to as chromatic aberrations, can decrease the performance of the system since the lack of local current matching may lead to lateral current flows, and thus resistive losses and increased recombination [5]. It is therefore instructive to measure the subcell irradiance profiles with our CPV-ACTT imaging system [8], that subcell current profiles may be calculated to more clearly reveal the POE temperature dependent impact of chromatic aberration on the systems under study. Subcell current profiles for a standard Spectrolab triple junction solar cell were generated from their external quantum efficiencies. Since the bottom subcell is significantly overproducing under realistic outdoor conditions, only profiles for the top and middle subcells need to be considered.

Subcell irradiance profiles have been measured for System 1 and are shown in the top row of Fig. 6, for the same temperatures range of $25^{\circ\,C}$ to $50^{\circ\,C}$. The x and y axis mark the location on the MJSC and the vertical axis is the photo-generated current in µA. Moving to the second row of Fig. 6, the profiles for the top subcell are shown in blue, and those for the middle in red. The significant profile difference reveals a pronounced chromatic aberration at each temperature. The bottom row of Fig. 6 shows the temperature evolution of the top-to-middle subcell current ratio profile. The color scale goes from blue (middle subcell overproduces) to green (top subcell overproduces), with red indicating local current matching. The progression from predominantly bluish to largely green is evidence of a strongly temperature dependent chromatic aberration. More specifically, when the mean current ratio are compared from 25° C to 55° C, there is an increase of 160% due to an reduced top and middle subcell current by 22% and 80%, respectively. The extensive color diversity at each temperature means strong lateral current flows and a greater temperature dependence for higher wavelengths.

Results similar to the above are shown in Fig. 7 for System 2, but the effect of the SOE is to significantly reduce the profile difference, compared to that of System 1. In particular, we see that at high temperatures, the SOE enables the dramatic recovery of the longer wavelength profile across the middle subcell. Furthermore, the temperature sensitivity of the chromatic aberrations minimized to a 10% and 6% increase in both the top and middle subcell profiles, respectively.The bottom row of Fig. 7 shows a weaker, but still not insignificant, temperature dependence to the chromatic aberration. Significant color diversity is still seen, but it is clear that the SOE reduces the impact of chromatic aberration.

The results for System 3, with the more advanced 4-FK design, are shown in Fig. 8. The profile difference continues to decrease, with a slight reduction over that of System 2, and marked improvement in profile uniformity. This results in slightly less temperature dependence to the chromatic aberration than found in System 2, with much less color diversity. Specifically, there is a minimal increase of 2% in the mean current ratio at remain top subcell limited for the full temperature range. This is clearly a design far superior to the other two with stable subcell profiles.

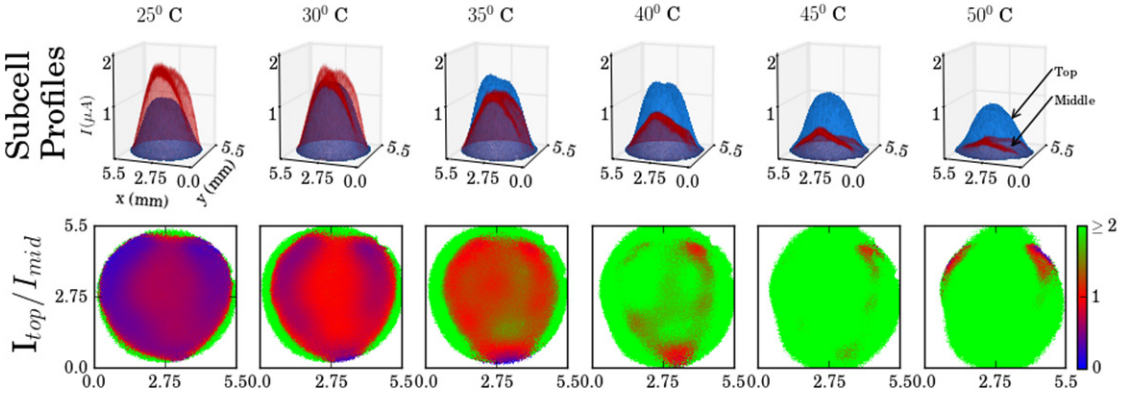

FIGURE 6. Top row – subcell irradiance profiles at the indicated System 1 POE temperatures for a SMR of 1.0; top subcell: blue, middle subcell: red. Bottom row – the corresponding Top/Middle subcell current ratio profiles.

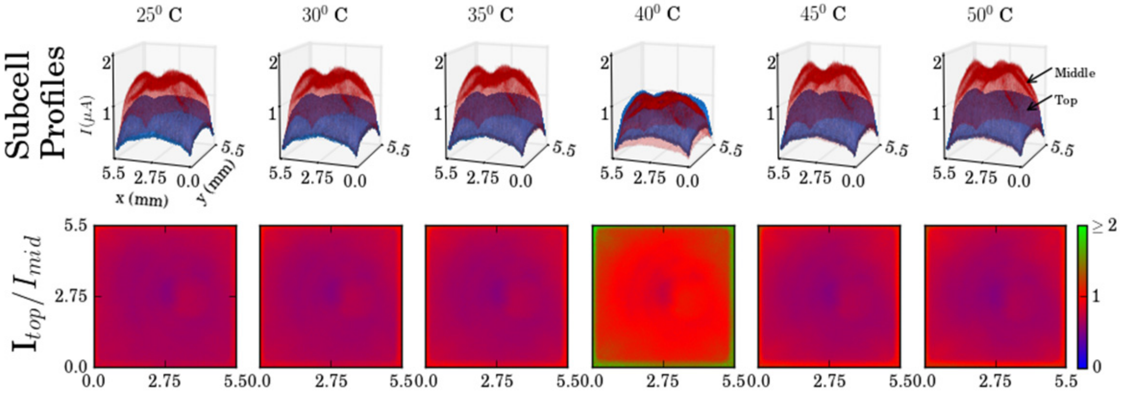

FIGURE 7. Top row – subcell irradiance profiles at the indicated System 2 POE temperatures for a SMR of 1.0; top subcell: blue, middle subcell: red. Bottom row – the corresponding Top/Middle subcell current ratio profiles.

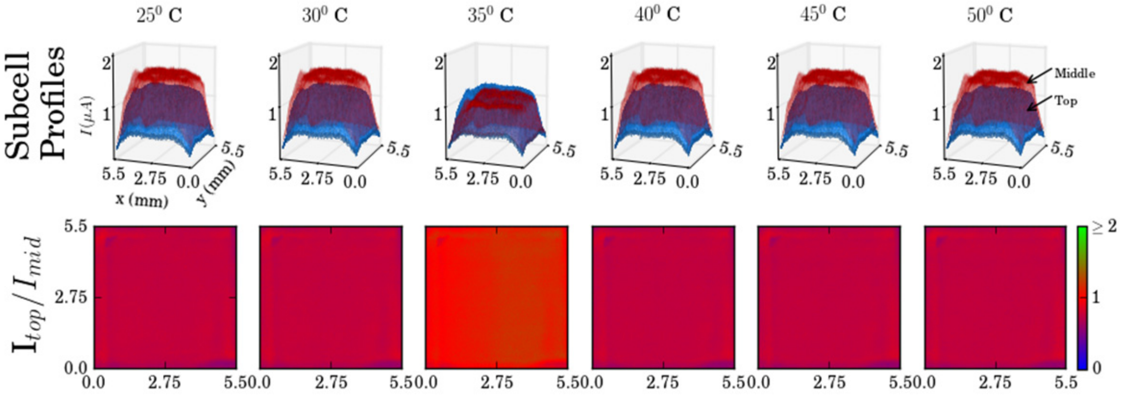

FIGURE 8. Top row – subcell irradiance profiles at the indicated System 3 POE temperatures for a SMR of 1.0; top subcell: blue, middle subcell: red. Bottom row – the corresponding Top/Middle subcell current ratio profiles.

Chapter 5

Detailed characterization of optics and system performance for three generations of CPV systems

5.1 Operating conditions and lens temperature impact on optical performance and annual energy yield across concentrator photovoltaic design space

5.1.1 Scope and contribution

The following publication is a study of how the different operating conditions affect the optical and system performance of three commercialized generation. We see that deployed systems are subject to three different operating conditions. Variations in cell to primary distances are introduced by manufacturing and module degradation. Optics are designed with specific acceptance angles, but even the smallest misalignment can have an effect on their performance. The temperature of the lens is never stable, thereby a system is often operating under non optimized conditions. The effect of these three situations on the irradiance profiles are quantified with the measurement technique discussed in Chapter 3.

It is also important to understand the long term effects of operating conditions on the output of the system. However, being in its early stages, long-term reliability and performance data are not available so annual outputs are calculated using different energy yield models. Our analysis further examines the instantaneous effects of how the lens temperature influences the energy yield calculation and how a system can profit from different cell to primary distances for a specific lens temperature distribution.

The measurements of the three systems were taken at CAE-INES in France with Dr. Besson. The quality control of the irradiance dataset was performed by Lianne de la Salle and myself, this work was put together in a conference proceeding for PVSC in 2016 led by Dr. Joan Haysom [B - 28]. All the post processing analysis and writing were done in Ottawa by the first author with editing help from the coauthors.

5.1.2 Publication

Patrick McVey White, Pierre Besson, Mathieu Baudrit, Henry Schriemer, and Karin Hinzer,“Operating conditions and lens temperature impact on optical performance and annual energy yield across concentrator photovoltaic design space,” advanced draft to be submitted to *Solar Energy*, October 2016.

Advanced draft attached on the next page.

Operating conditions and lens temperature impact on optical performance and annual energy yield across concentrator photovoltaic design space

Patrick McVey White,[a,*] Pierre Besson,[b] Mathieu Baudrit,[b] Henry Schriemer,[a] and Karin Hinzer[a]

[a] *SUNLAB, Centre for Research in Photonics, University of Ottawa, Ottawa, Canada*
[b] *CEA-LITEN, LCPV, INES, Le Bourget du Lac, France*

Submitted 26 September 2016

Abstract

Operating conditions of an outdoor concentrator photovoltaics module is subject to fluctuations varying its output. From the first generation with only a Fresnel lens, two newer architectures have been commercialized showing greater stability for variations in cell to primary distance, misalignment, and lens temperature. The total irradiance of a bare Fresnel is reduced by 30, 38, and 22% for the three mentioned conditions, respectively. The truncated inverted pyramid secondary, second generation, help degrees the influence of the operating conditions but the 4 Fresnel-Kohler, latest generations, showed the best performance with a change of only 2, 4, and 3%. The increase in the stability of the output simplifies the annual energy yield calculations. The annual output only differs by 0.5% absolute when comparing a single versus temperature influence efficiency for the third generation using ground measured data. An improvement to the first and second generation, which had a difference of 9.4, and 1.7. The difference in energy yield calculations based on the satellite date showed the same order of magnitude.

Keywords: Concentrator photovoltaics; Optical performance; Energy yield calculation; Concentrator standard test conditions; Silicon on glass Fresnel lens; Polymethylmethacrylate Fresnel lens; 4 Fresnel- Köhler; Temperature dependence measurement

---

1. Introduction

The principle of concentrator photovoltaics (CPV) is to focus light by means of optics onto high efficiency multi-junction solar cells (MJSC). By leveraging inexpensive optical materials, typically silicon-on-glass (SoG) or polymethylmethacrylate (PMMA), a larger optical-to-cell area offsets the MJSC footprint. Using new optical designs in conjunction with the high efficiencies of MJSC [1], CPV systems display high yearly power output [2, 3].

For refractive concentrating systems, there have been three distinct generations in architecture improving on efficiency, reliability, and cost [4]. The first generation is the classic and simple approach of an imaging optic, typically a Fresnel design, with no secondary. Without a secondary, there is nonuniform distribution of the high irradiance and consequently lower tolerances, which diminishes the performance of a MJSC due to series resistance and lateral current flow within the individual subcells [4, 5, 6, 7, 8]. The second generation improves performance by using a simple nonimaging secondary to increase homogeneity across the MJSC and to improve module acceptance angle. Finally, third generation designs have led to complex optics that break the rotational symmetries of previous generations, with asymmetric free forms used to achieve higher performance levels [3, 9]. All three generations are used in ongoing and new CPV deployments. These systems are subject to a variety of different operating conditions, including, but not limited to, tracker misalignment, cell-to-primary distance, and lens temperature. The goal of this article is to investigate and quantify the influence of these three conditions on the irradiance profiles for these three generations.

Due to imperfections, chromatic dispersion, and temperature dependencies of primary materials, optical performance varies with operating conditions. The first section discusses how these conditions are simulated and describes the method used to determine the irradiance profile on the cell. The second section contains three subsections, one per operating condition. Manufacturing tolerances and physical bowing of the lens over time are sources that can change the optimized cell-to-primary distance. It has been shown, by Victoria *et al*. [6], that this can decrease the efficiency by 6%. The first part of the second section will discusses the influence of cell-to-primary distance on irradiance profiles. Since modules tracking errors can approach incident angles up to 3° [10], far greater than the ±1° acceptance angle of a CPV system, the second part will analyze the effect of different incident angles on the irradiance profile. The third part will focus on the impact of lens temperature variation, which drives thermal expansion, and consequently changes in the focal distance, reduced concentration, and Fresnel facet deformation [11, 12, 13, 14]. We address how such changes impact individual subcell response, to analyse and compare the effect at the system level. Additionally, the sensitivity of annual mean efficiency to temperature-driven variations in cell-to-primary distance will investigated to determine an optimal distance for specific lens temperature distributions. A temperature influence efficiency map will be used to compare the output of energy yield calculations with and without lens temperature variations. We use data from Ottawa, Canada, where the ambient temperature ranges from -30 to 40 °C.

2. Experimental technique for CPV optics

2.1. CPV optical architectures

Three generations (Gen) of commercially available systems are studied: Gen 1 – a SoG Fresnel primary without any secondary; Gen 2 – a PMMA Fresnel primary with a truncated-inverted-pyramid (TIP) secondary; and Gen 3 – a four quadrant Fresnel-Köhler (4-FK) system. The primary used for Gen 1 is a Fresnel design with 5.7 cm sides and a geometric concentration ratio of 500. Gen 2 has a similar primary, 20 cm sides but a larger surface area, for a geometric concentration ratio of 820; its secondary uses total internal reflection from planar faces to generate multiple images of the entire primary across the MJSC in an effort to increase uniformity. The Gen 3 system has a PMMA primary with 16 cm sides and a geometric concentration of 710. Four independent Köhler channels are produced by the primary, thereby reducing the field of view onto the nonplanar faces of the secondary, where Köhler integration images each channel independently onto the MJSC. The result is performance levels superior to those of earlier generations [2,8]. The three systems are summarized in Table 1, with their basic ray tracing schematics given in Fig. 1.

Table I Summary of material and design of CPV optical elements

Generation	Primary			Secondary	
	Material	Design	Concentration	Material	Design
1	SoG	Fresnel	500	N/A	N/A
2	PMMA	Fresnel	820	Borosilicate glass	Total internal reflection
3	PMMA	Four-unit Fresnel array	710	Borosilicate glass	Köhler integration

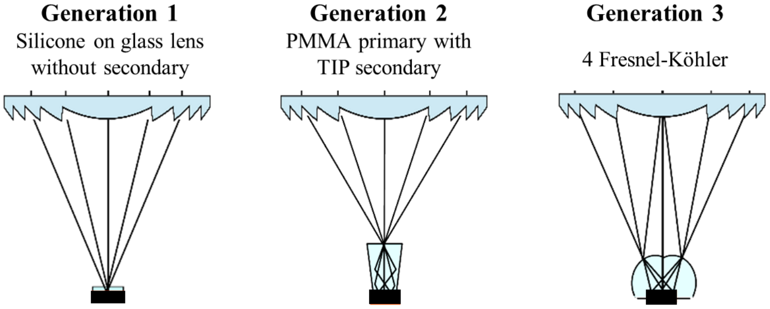

Fig. 1. 2-D ray tracing diagrams for three generations of CPV optics: a silicone-on-glass Fresnel lens without a secondary optic, a PMMA Fresnel lens with a truncated inverted pyramid secondary optic, and a 4 Fresnel-Köhler system. The black bar shows where the cell would be placed – that is, where the optical profile is imaged.

2.2. Optical imaging of CPV systems

Due to MJSC spectral sensitivity, is necessary to spectrally image the optics' irradiance profile to understand its impact. Within a CPV solar simulator, we have constructed an automated thermal test-bench, which consists of a thermal chamber to isolate the primary lens, and an optical imaging system. The temperature and humidity within the chamber are controlled with an automated closed loop feedback system via sensors placed on the lens. The chamber encloses the lens within highly transparent glass windows, with the output focused externally onto an opal diffuser, located at the nominal MJSC position. This identifies an equivalent image plane where the full irradiance profile and chromatic aberration, otherwise seen by the top of the MJSC, can now be measured. A spectral profile from 350 nm to 1000 nm is reconstructed from an imaging system that uses a CMOS detector coupled with twelve bandpass filters, achieving 50 nm resolution. From the broadband irradiance profile, the subcell profiles can be calculated for any MJSC given its external quantum efficiency. The bottom subcell profile is not considered since the germanium layer in a triple junctions solar cell is designed to overproduce current under to compensate for a poor fill factor. Using this characterization technique, the subcell current distribution can be quantified within 2% and 3%, for the top and middle subcell, respectively [10].

3. Effects of operating conditions on solar cell surface irradiance profiles

3.1 Cell to primary distance

Since chromatic aberration creates a spectrally-dependent focal distance, variations in this distance affect the optical uniformity across the image plane. The optimal cell-to-primary distance may be identified with the position that maximizes total power. Under standard test conditions (STC – 25°C), the distances were experimentally determined as 195 mm for Gen 1, 149 mm for Gen 2, and 261 mm for Gen 3. Fig. 2 shows normalized irradiance distributions for optimal cell-to-primary distances (central column), and for departures of ±2 and ±4% from their nominal distances (positive values implying larger distances); these departures are consistent with variations that can be induced by lens warping over time. Gen 1 (top row) is seen to have the most inhomogeneous profile, with peak shape strongly dependent on cell-to-primary distance, ranging from a narrow mesa at large distances (+4%) to more sharply peaked as short distances (-4%). Ray tracing also shows this increasing peak-to average ratio as the distance is decreased, with greater ray confinement to the imaging surface than at the larger distances, where total irradiance is more strongly reduced. Gen 2 (middle row) shows much flatter optical profiles than does Gen 1, even at the extreme departures from optimal positioning. The structure in these profiles is due to the square symmetry of the secondary optic. Again, ray tracing reveals that profiles at larger distances see greater homogenization due to an overall increase in the number of sidewall reflections, but with reduced total irradiance due to overfilling the entry aperture and increasing loss of total internal reflection. Gen 3 (bottom row) demonstrates a very homogeneous profile that is largely insensitive to changes in the cell-to-primary distance. The four quadrant Fresnel-Köhler design has effectively suppressed the influence of any fourfold structural symmetry by optimizing the secondary surface orientation at each point across an individual quadrant vis-à-vis its Fresnel primary. By comparison with earlier generations, ray tracing reveals greater uniformity in the ray bundles and consequently far less variation in total irradiance with changing cell-to-primary distance (from a 4% decrease at -4% to a 6% increase at +4%), with no more than a 2% variation in peak to average ratio in any Gen 3 profile.

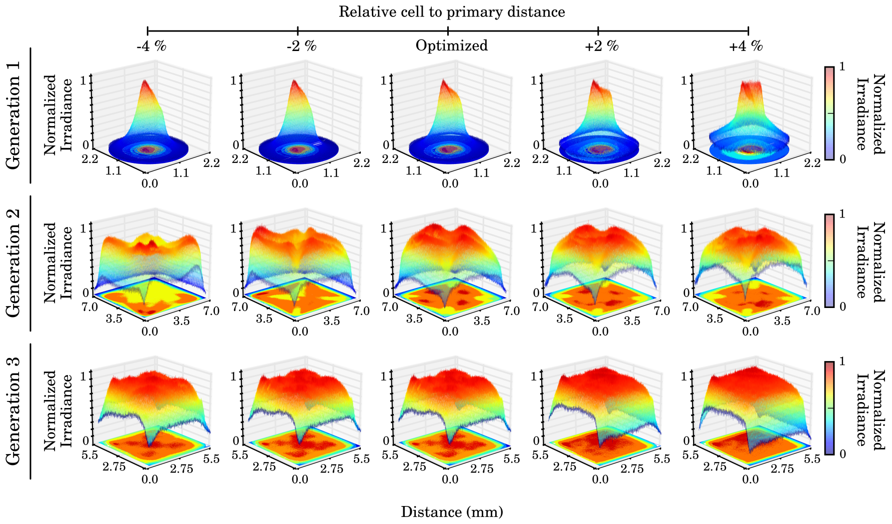

Fig. 2. Effect of cell-to-primary distance on the irradiance profile measured for the three generations.

3.2 Angle of incidence

The acceptance angle is fundamentally constrained by the optical concentration, as expressed through the concentration acceptance angle product (CAP), as consequence of the conservation of etendue [4]. Nominally then, higher concentration modules are more susceptible to tracking errors, so we expect Gen 2 (see Table I) to be the most sensitive to module misalignment, and Gen 1 the least, but concentrator architecture does play a role [8]. To assess this, we have measured the irradiance profile for each module with increasing angle of incidence (*i.e.*, misalignment angle). The evolution of the normalized irradiance profiles, from near-on-axis to 1° misalignment, is shown in Fig. 3 for all generations. The irradiance profile of Gen 1 (upper row) is most sensitive to misalignment, the strongly localized focus showing a marked lateral shift with increasing misalignment angle. The peak to average ratio is found to remain constant until 0.5°, but thereafter increase, and by 1° misalignment, there is a 40% loss in intensity, and a 50% increase in the peak to average ratio. The peak is seen to fall off the nominal cell surface at a 0.6° misalignment, where the 10% reduction from the aligned intensity means that this is the Gen 1 acceptance angle. By contrast, the acceptance angles of Gen 2 (middle row) and Gen 3 (bottom row) are found to be 0.8° and 1°, respectively, which are both higher than that found for the lower concentration Gen 1, demonstrating the profound impact that concentrator architecture has on acceptance angle. Gen 2 has slightly higher concentration than Gen 3 (see Table I), so its slightly lower acceptance angle elicits no surprise. However, Gen 2 leads to better electrical performance than Gen 3 because its irradiance uniformity is superior to that of Gen 3 at these higher angles [8]. For Gen 2, at 1° misalignment, the change in peak to average ratio is less than 1%, but the optical intensity has only decreased by 14%; by contrast, the peak to average ratio for Gen 3 has increased by 20%, more than offsetting the lesser 10% decrease in its optical intensity. The 4 Fresnel-Köhler design is superior only near normal incidence, where each Köhler channel links primary and secondary optics; misalignment leads to "crosstalk" between channels and greater profile nonuniformity [8]. Thus, profile evolution should be more carefully considered when evaluating CPV system technologies for energy yields.

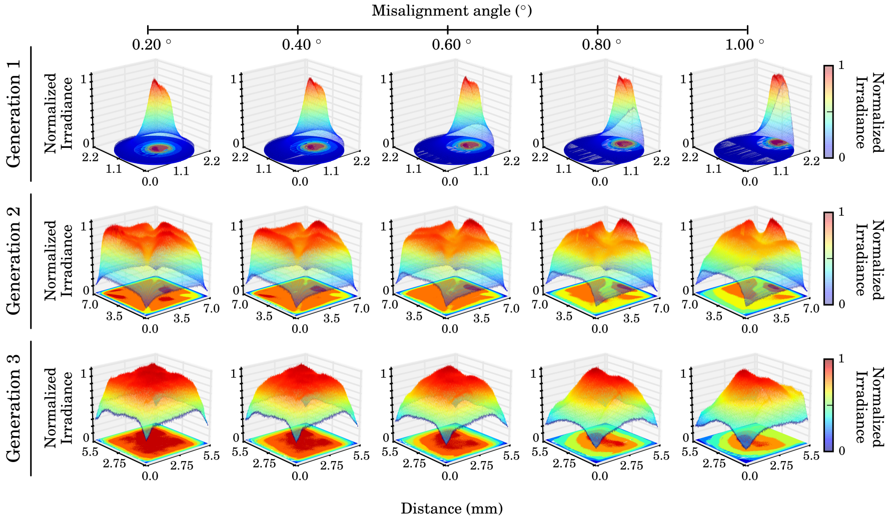

Fig. 3 Effect of on the irradiance profile measured and every 0.10 ° from 0.00 ° to 1.00 ° for each of the three generations.

3.3 Primary lens temperature

Fig. 4 has the irradiance profile, subcell current profile, and the top to middle current ratio for all three generations labelled on the left. For each profile, the results are shown at every 10 °C from 25 °C to 55 °C. The irradiance is the integration of the 50nm resolution spectrum from 350 to 1000nm and is in kW/m^2. Below, the current profile of the top, blue, and middle, red, subcells that where calculated from the measured external quantum efficiency of a standard triple junction Spectrolab cell. Finally, the top subcell divided by the middle subcell profile gives the current ratio distribution of the cell where the regions highlighted are blue, green, and red where the areas represent when the MJSC is top subcell limited, middle subcell limited, and current matched, respectively.

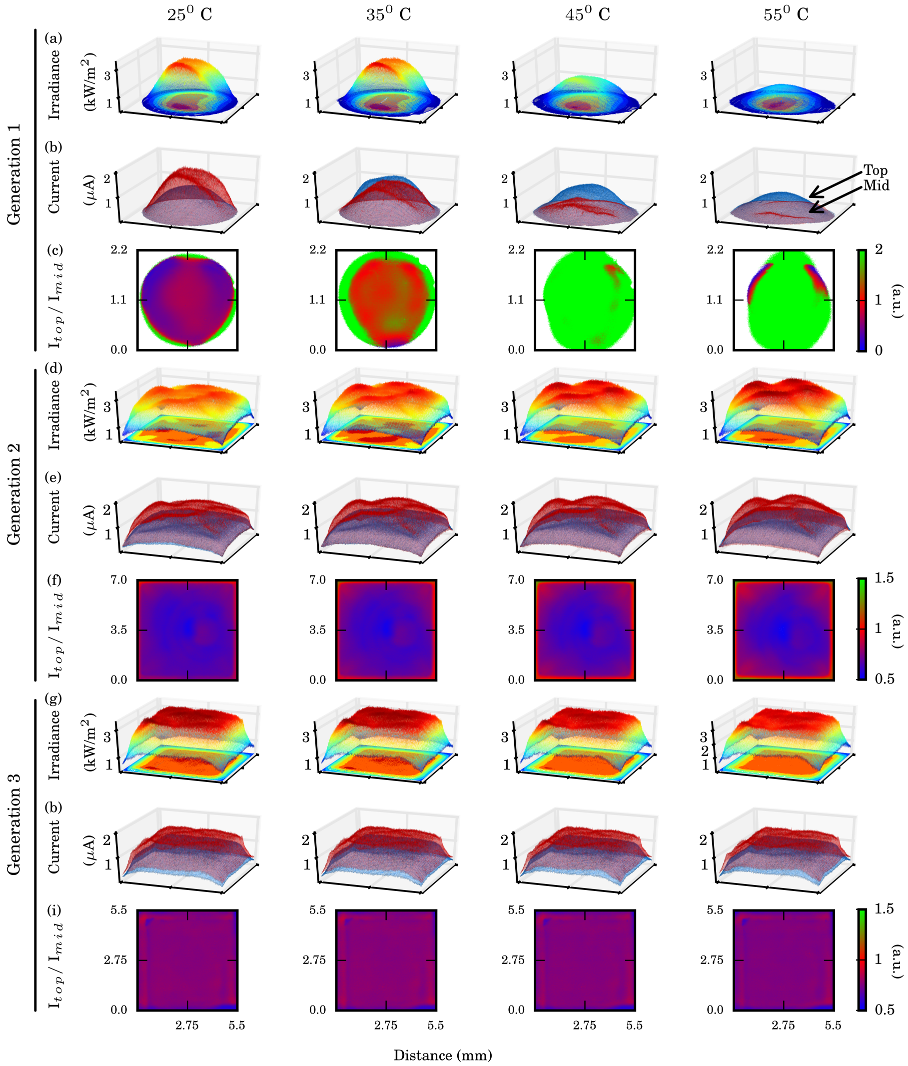

Fig. 4. Effect of lens temperature on the irradiance profiles, top and middle subcell current profiles, and top to middle current map for generation 1, 2, and 3. The subcell profiles are calculated from the measured external quantum efficiency of a standard triple junction Spectrolab latice matched triple junction solar cell. The images are captured under a filtered CPV xenon flash solar simulator with a top to middle spectral match ratio of 1.0.

Starting with the CSTC conditions, the first column, Gen 1 is top subcell limiting where there is 45% more current in the middle subcell spectral band, seen in Fig. 4 (b). Looking at Fig. 4 (c) at 25 °C, there will be significant lateral current flow within the middle subcell on the outer edges. Heating the lens my 10 °C results in an increase of 5% in the total irradiance and 55% in the top subcell. With a decrease in the middle subcell, the system has a higher degree current matching, which should result in a better performance from the cell. However, as the lens temperature is father increased, it is evident that the higher wavelengths are more sensitive with a drastic decrease in the middle subcell by 90% but only 22% in the top subcell from 25 °C to 55 °C. These results show that a bare Fresnel lens is extremely sensitive to lens temperature with a higher degree of chromatic aberration at higher temperatures.

Fig. 4 (d)-(f) shows an increase in the uniformity of the irradiance and subcell distribution for Gen 2. As the primary is heated, we see an increase of 16% in the total irradiance, darkening of the peaks in Fig. 4 (d). Unlike the results seen for varying cell to primary distance, which have a similar principle where the focal point is shifted in respect to the aperture opening, as the lens is heated there is actually an increase in the focal distance of the lens.

This results in a decrease in the incident angle of the rays with the secondary, reducing reflection losses and increasing the irradiance on the cell. The increase breaks down into 12% and 8% in the top and middle subcell spectral bands, respectively. A significant improvement in comparison to the effects seen in Gen 1 when Gen 2 should have better performance at higher lens temperature. For the full temperature range the peak to average increase by only 2% while the MJSC remains top subcell limited. The stability of the current ratio, seen in Fig. 4 (f), is a direct result of the secondary and decreases the sensitivity of the system to different lens temperatures.

Gen 3 in Fig. 4 shows superior uniformity in the irradiance profile as the lens temperature is heated. In comparison with 25 °C, the total irradiance does however decrease by 4% when the top and middle decrease by 5% and 3%, respectively. The uniformity across the cell does not change due to the Fresnel-Köhler channels principle. By dividing the incident rays into bundles means that each channel will have a smaller degree of amplification and the 4 images of the primary are superimposed at the cell where any changes in the primary will be reduced at the cell level. Therefore, in comparing the three generation we see that both Gen 2 and 3 reduce the influence of lens temperature on the optical performance. The addition of the secondary for Gen 2 means the change in focal distance of the rays from the primary, originally losses in Gen 1, are captured and there is actually in increase in performance at higher temperature. Finally, Gen 3 shows the most stable output and the CSTC conditions are representative of the system over the full lens temperature range measured.

4. Influence of lens temperature on annual energy yield calculations

The direct energy yield calculation requires a measured irradiance value at each timestamp. This is computationally heavy especially when the system efficiency has to be calculated at each point with an irradiance, wind speed, and ambient temperature value. Yandt et al. [18] simplified this calculation by using the local air mass as a spectral proxy to bin the irradiance value. This method works since every time the same air mass occurred, the system efficiency would be the same. With the principle, we can use the lens temperature as a proxy where the energy output can be calculated for each lens temperature rather than each timestamp. The lens temperature can be estimated based on ambient temperature, direct solar irradiance, and wind speed for a Fresnel based system according to the following equation:

$$\mathrm{T}_{lens} = \mathrm{T}_{ambient} + m_l * \left[\exp\left(-\frac{1}{2} * \frac{v}{v_o}\right) + c\right] * I_{DNI} \tag{1}$$

where T_{lens} is the lens temperature, $\mathrm{T}_{ambient}$ is the ambient temperature, m_l is 2.279 10^{-2} K m^2/W for a Fresnel lens, v_o is 0.198 m/s, c is 0.5891, and I_{DNI} is the irradiance in W/m^2 [11]. The irradiance and wind speed, missing variable in Eq. 1, were provided by the SUNlab and SolarAnywhere® to perform the energy yield calculations based on validated ground data [18] and satellite data [15], respectively. Returning to lens temperature as a proxy, Fig. 5 shows the cumulative annual direct normal irradiance energy distribution as a function of the ambient and lens temperatures for a Fresnel-based concentrator system installed in Ottawa (Lat: 45.42 °, Long: -75.69 °, Elv: 70 m). Comparing the ambient temperature distributions, the mean bias error of the satellite data is 8.6%. However, this error is reduced to 2.8% when the ground measurement, which has a 2 minute resolution, is averaged over an hour to match the resolution of the satellite data. Additionally, the difference between the two datasets is 202.3 kKh/m^2 on the full year.

In order to perform the energy yield calculation that includes the effect of lens temperature, we need the system efficiencies as a function of lens temperature. The efficiency maps, which is a function of lens temperature and relative cell to primary distance, can be seen for the three generations in Fig. 6 where the lens temperature ranges from 25 to 55 °C and the cell to primary distance ranges from ±4 % relative to the optimized distance. The efficiency was measured under the same Xenon flash lap from the previous section. The spectrum was measured simultaneously where the efficiencies plotted in Fig. 6 all have an incident spectrum where the spectral mismatch ratio was 1, now, let's look at how the system efficiencies are affected by lens temperature and cell to primary distance.

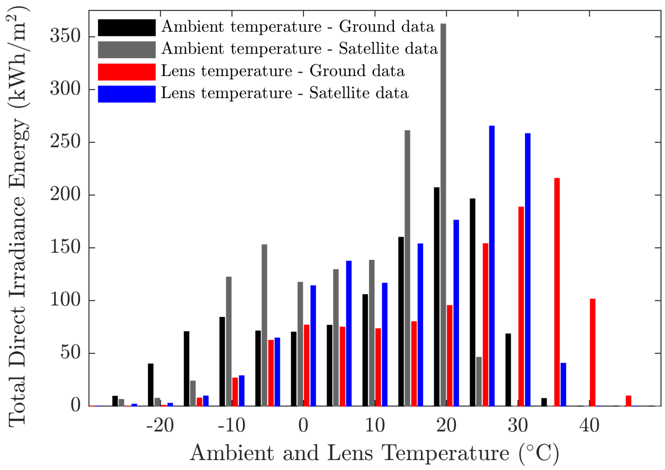

Fig. 5. Cumulative annual direct normal irradiance energy distribution binned for every 5 °C difference in lens temperature. Lens temperatures are calculated from ground and satellite data for a Fresnel lens based concentrator photovoltaic system installed in Ottawa, Canada (Lat: 45.42 °, Long: -75.69 °, Elv: 70 m).

The optical performance of Gen 1 was influenced quite drastically when the operating conditions were varied and we see the same thing in the system efficiency shown in Fig. 6 (a). Starting with the efficiency curve for the relative cell to primary distance, there is a relative increase in efficiency of 2.5% between 25 and 35 °C. If we refer back to the optical performance, heating the lens to 35 °C created a higher degree of current balance between the top and middle subcell, which results in less lateral current flow in the middle subcell leading to the better cell performance. The efficiency values in Fig. 6 (a) shows that Gen 1 is competitive with Even though there is a higher peak to average ratio for Gen 1, the system efficiencies, under optimized conditions, is competitive with its successors. This results agrees with Korech [19], where reducing the cell area decrease the total photocurrent and front grid resistance under high flux non-uniform. Therefore, the dominating losses are in the reduction of irradiance, due to rays exceeding the surface of the MJSC, and chromatic aberrations, causing lateral current flows within the subcell. Comparing the individual efficiency curves as a function of temperature for different cell to primary distance there is an interesting trend. Starting at +4 % and moving to +2% the peak efficiency shift toward lower temperatures and the same occurs moving to the relative, -2 % and – 4 %. In the previous section, when the cell to primary distance was increased, there was a decrease in irradiance but as the temperature increases so does the focal distance of the lens. Therefore, the same irradiance distribution will occur and in reference to Fig. 6 (a), the efficiency values at the coordinates (+2 %, 45 °C), (0 %, 35 °C), and (-2 %, 25 °C), which can also be seen by the red areas of the contour plot. Moving away from these irradiance profiles, there is an absolute decrease in efficiency of 16.9 and 14.6 % for the blue area of the contour plots.

Looking at the effects on the efficiency maps of Gen 2 and Gen 3, Fig. 6 (b) and (c), respectively, there is a clear decrease in the influence of operating conditions. For Gen 2, we see a symmetry about the relative focal distance and a lens temperature of 40 °C. Along the relative focal distance, there less than 1% decrease in absolute efficiency due to lens temperature. If the cell to distance is increased by 2% there is a drop of 2.2 % then 6.1% at 4%. In the other direct, the efficiency is decreased in same of magnitude for –4 % but at -2 % the system favors higher lens temperature as there is an increase of 1.1% in the absolute efficiency from 25 °C. In summary, the system output is stable when the cell is at its optimal distance from the primary for all lens temperature values. On the other hand, a small change of 2% causes the output to decrease and become instable as the lens temperature changes. Fig. 6 (c) shows the system performance of Gen 3 over varying operating conditions is extremely stable. Increasing the lens temperature results in a decreases in the absolute efficiency by less than 1 %, regardless of the cell to primary distance. At a specific temperature, the output when the cell to primary distance is stable for the cell to primary distances above the optimized distance. However, decreasing the distance by 2 or 4 % results in a 0.6 and 1.6% decrease in absolute efficiency, respectively.

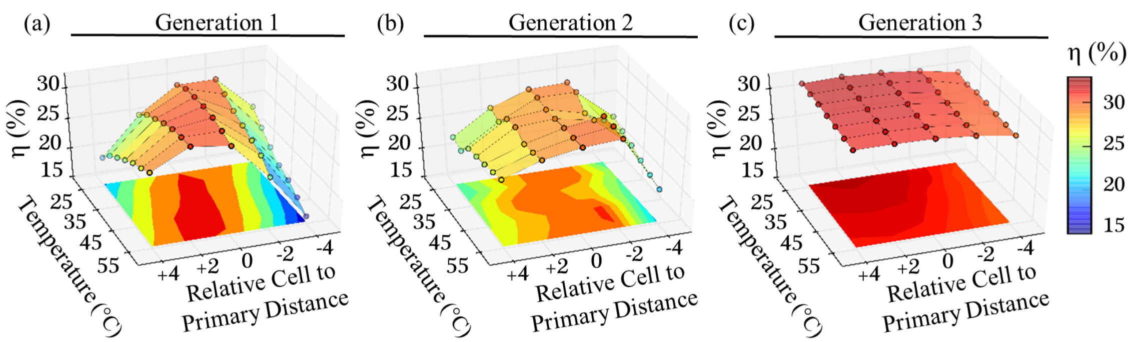

Fig. 6 Efficiency map showing the infleunce of lens temperature, from 25°C to 55°C, and cell to primary distance, ±4 and ±2% of the focal distance, for the three generations.

To clearly show the influence that lens temperature has on the energy yield, we will compare the outputs when the calcualtions are done using the efficiency curve along the relative cell to primary distance from Fig. 6 and the single efficiency value measured under the CSTC standards, lens and cell temperature of 25 °C. Fig. 7 shows the difference between these two calculation for the three generations. The calculation for Gen 1 results in a realtive difference of 9.4 %, equivalently 31.44 kW/m^2. Additionally, the distribution of Gen 1 in Fig. 7 shows that for regardless the lens temperature a single efficiency value is not representative to the performance of the system under the varied operating condition especially at lower lens temperatures. On the other hand, the effect of lens temperature on the energy yield calculations for both Gen 2 and 3 results in a relative difference of 1.7 and 0.5 %, respectively. Even though the single efficiency values seen in Fig. 6 (b) did not have a significant difference between lens temperatures, when the total irradiance is considered, the effect becomes more pronounced. The temperature range where the energy yield calculations has the highest bias when the lens temperature is at 40 °C with a difference of 744 W/m^2. The difference between the calculations for Gen 3 saw the lowest bias of 95 W/m^2. The results shown in Fig. 7 shows that lens temperature can still change the annual output when comparted to a single efficiency value. However, the procession of the generations greatly diminishes the difference.

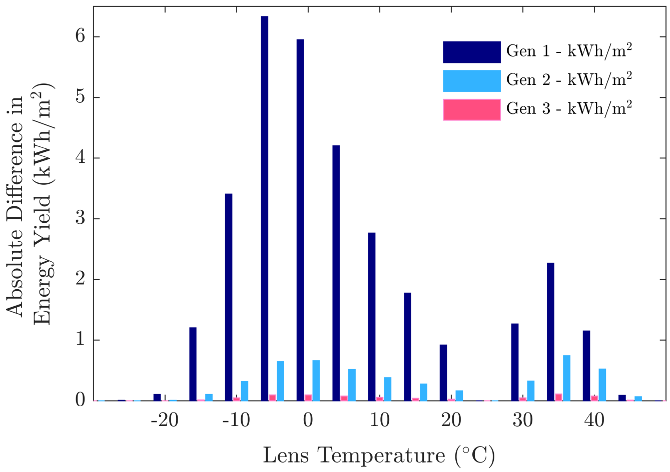

Fig. 7 Distribution of difference in cumulative annual energy yield calculation between a single and temperature influenced efficiency value. The energy energy is binned for every 5 °C difference in lens temperature calculated for ground measured irradiance values in Ottawa, Canada.

It should be noted that the annual output for the lens temperature calculation was based on the ground measurement distribution in Fig. 5. The difference between the calculation for the satellite data can be found in Tab. 2. The satalite data consistantly over biases the relative difference. However, this only results in an absolute difference of 1.8, 0.4, and 0.1 % for Gen 1, 2, and 3, respectively. Refering back to Fig. 5, we see the same trend in the irradiance distribution causing this difference.

Table 2
Relative percent difference in annual energy yield calculation between a single and temperature influencing efficiency values for the three generations using ground and satellite data.

	2 min. steps	1 hr. steps	
Generation	Ground (%)	Ground (%)	Satellite (%)
1	9.4	10.4	12.2
2	1.7	1.8	2.2
3	0.5	0.5	0.6

5. System optimization to minimizing annual effects of lens temperature

Understanding the effects of operating conditions on system output can be advantageous to optimize the performance depending on a specific location or locations with similar characteristics. Let's look at how we can optimize the three generations for Ottawa, a location with an energy distribution that favors lower temperatures.

Fig. 8 shows the annual mean efficiency of the three generations as a function of the relative cell to primary distance, which was optimized under the CTSC conditions. The mean efficiency was calculated by averaging the lens temperature influenced efficiency over one year, thereby considering the energy distribution shown in Fig. 5 for both the ground and satellite data. In comparison, Fig. 8 (b) shows 1% absolute bias in the efficiency calculation when the satellite data is used. The larger variations seen for Gen 1 and 2 since their efficiency curves as a function of temperature were different depending on the cell to primary distance. On the other hand, Gen 3 exhibited nearly identical efficiency values for each cell to primary distance.

In reference to Fig. 8 (a), Gen 1 and Gen 3 can be optimized to increase their efficiency. Although almost identical for each cell to primary distance, increasing the cell to primary distance by 2 % results in a relative efficiency gain of 2.5%, increasing the total output. Extrapolating to long-term performance, another advantage by increasing the distance prevent future losses due to any warping of the module. Optimizing the position of the cell in a Gen 1 module can increase the efficiency 26.9% relative, an absolute increase of 6.7%. Additionally, under these conditions, is a competitive option to a Gen 3 module. On the other hand, the optimized position for a Gen 2 module remains the same where an increase or decrease results in a relative loss of 3.4%.

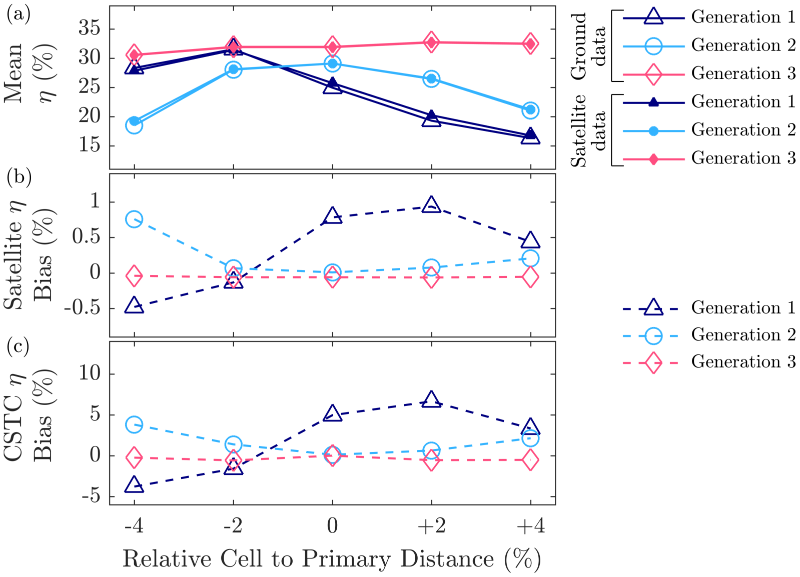

Fig. 8 (a) Effect of cell to primary distance on annual mean efficiency compared to the efficiency measured at the CSTC testing conditions, dashed line, for both ground and satelite data for the three generations. (b) The difference between the efficiency values from the ground to sattelite data. (c) The difference between the temperature influenced annual mean and efficiency measured at the CSTC testing condition.

Fig. 8 (c) compares the efficiency values for the three generations measured under the CSTC standards to the annual mean efficiency values. For Gen 1, a single efficiency value is not representative of the annual performance when the lens temperature is considered. However, under the optimized cell to primary distance seen in Fig. 8 (a), there is only an absolute difference of 1.6% but can reach up to 5.0%, if the cell to primary distance is optimized under the CSTC conditions. On the other hand, the CSTC conditions are representative for Gen 2 and 3 with a difference in absolute efficiency of less than 0.5 % and 0.1%, respectively. The advantage of Gen 3 is the stability to both lens temperature and cell to primary distance and it is evident that each new generation has improved on the performance of its predecessors. Therefore, simplifying the energy yield calculations since a single efficiency value, set by the international standards, is representative of the systems output under operating conditions.

5. Conclusions

Through spectrally imaging of a CPV modules irradiance profile, we have quantified the effects of operating conditions on the optical performance of the three generations of CPV designs. We have taken three commercialized system as a representative candidates for the individual generations. The first generation, a silicone on glass Fresnel lens without a secondary optic, was the most susceptible to cell to primary distance, misalignment, and lens temperature, the three operating conditions or interest in this article. At the extremes of the three aforementioned conditions the irradiance on the MJSC was decreased by 30, 38, and 22 and an effects on the same order of magnitude with the peak to average ratio. The issue with the first generation is without a secondary, any effect altering the rays exciting the primary or incident on the MJSC have a direct cause and effect. The second generation uses total internal reflection within a truncated inverted pyramid to help mitigate the effects of operating condition. There is a drastic improvement with a 13, 14, and 16 % change in the irradiance. Finally, the third generation implements free form optical design breaking the symmetry of the previous generations where the primary and secondary are designed together and reduces the effects of operating conditions by one order of magnitude.

We have undertaken a study of how lens temperature can change the output of an energy yield calculation by comparing the results using a single and temperature dependent efficiency value. If the lens temperature is included, we see a difference of 9.4, 1.7, and 0.5% in the energy yield calculations for generation 1, 2, and 3, respectively, based on ground measured irradiance. Additionally, this calculation was performed with satellite data with only a bias of 2.8, 0.5, and 0.1 % is introduced. While our results showed a greater effect in the first generation, we also noted that the losses due to lens temperature can be reduced by approaching the cell to primary distance by 2% since there is an absolute gain 6.7% in the efficacy. On the other hand, the two most recent generation do not show significant improvement in performance my optimizing the cell to primary distance with lens temperature. This is a positive outcome since the performance is stable to varying operating conditions.

Acknowledgments

The authors would like to thank the LCPV research team at CAE-INES lab in France for their facilities and guidance. More specifically, Clement Wieck for assisting in the electrical and optical measurements. Partial funding from the European Union's Horizon 2020 research and innovation program within the project CPVMatch under grant agreement No 640873, the Natural Science and Engineering Research Council of Canada (NSERC), Ontario Centers of Excellence, and the Canada Research Chairs program are acknowledged.

References

[1] NREL, "Research cell efficiency records, NREL," (2016)

[2] J. Haysom, O. Jafarieh, H. Anis, K. Hinzer, and D. Wright, "Learning curve analysis of concentrated photovoltaic systems," Prog. Photovolt. Res. Appl **23** (6), 1678 - 1686 (2015).

[3] M. Muller, S. Kurtz, M. Steiner, G. Siefer, "Translating outdoor CPV I–V measurements to a CSTC power rating and the associated uncertainty" Prog. Photovolt. Res. Appl **23** (11), 1557-1571 (2015).

[4] A. Gombert, J. C. Miñano, P. Benitez, and T. Hornung, "Concentrator optics for photovoltaic systems, in Photon management in solar cells," (eds R. B. Wehrspohn, U. Rau and A. Gombert), Wiley-VCH Verlag GmbH & Co. KGaA (2015)

[5] P. Sharma, A.H. Trojnar, M. Wilkins, A.W. Walker, H. Schriemer, and K. Hinzer, "Comparative analysis of nonuniform illumination and chromatic aberration in triple and quadruple junction solar cells under concentration using SPICE," IEEE 29th Photovoltaic Specialist Conference, New Orleans (2015).

[6] M. Victoria, R. Herrero, C. Domínguez, I. Antón, S. Askins, G. Sala, "Characterization of the spatial distribution of irradiance and spectrum in concentrating photovoltaic systems and their effect on multi-junction solar cells," Prog. Photovolt. Res. Appl **21** (3), 308-318 (2013).

[7] H. Baig, K. C. Heasman and T. K. Mallick, "Non-uniform illumination in concentrating solar cells," Renew. Sust. Energ. Rev., **16**, 5890-5909 (2012).I. Garciá, P. Espinet-González, I. Rey-Stolle, and C. Algora, "Analysis of chromatic aberration effects in triple-junction solar cells using advanced distribution models," IEEE J. Photovolt. **1** (2), 219-224 (2011).

[8] P. Benítez, J.C. Miñano, P. Zamora, R. Mohedano, A. Cvetkovic, M. Buljan, J. Chaves, M. Hernández, "High performance Fresnel-based photovoltaic concentrator," Opt. Express **18** (1), 25-40 (2010).

[9] J. P. D. Cook, P. Sharma, L. de la Salle, F. Carle, P. McVey White, V. Tatsiankou, J. E. Haysom, E. Dragomirescu, H. Schriemer and K. Hinzer, “Refractive concentrator optics architectures, tracker precision, and cumulative energy harvest,” IEEE 29th Photovoltaic Specialist Conference, New Orleans (2015).

[10] T. Schult, M. Neubauer, Y. Bessler, P. Nitz, A. Gombert, “Temperature and wavelength dependence measurement and simulation of Fresnel lenses for concentrating photovoltaics,” 2nd International Workshop on Concentrating Photovoltaic Optics and Power, Germany. (2009).

[11] T. Hornung, M. Steiner, P. Nitz, “Estimation of influence of Fresnel lens temperature on energy generation of a concentrator photovoltaic system,” Sol. Energy Mater. Sol. Cells **99** (1), 333-338 (2012).

[12] S. Askins, M. Victoria, R. Herrero, C. Domínguez, I. Antón, G. Sela, “Effects of temperature on hybrid lens performance,” AIP Conf. Proc. **1407**, 57 (2011).

[13] V.D.Rumyantsev, N.Yu.Davidyuk, E.A.Ionova, P.V.Pokrovskiy, N.A.Sadchikov, V.M.Andreev, “Thermal Regimes of Fresnel Lenses and Cells in ”All-Glass” HCPV Modules,” AIP Conf. Proc. **1277**, 89 (2010).

[14] P. Besson, P. McVey White, C. Domínguez, P. Voarino, P. Garcia-Linares, M. Lemiti, H. Schriemer, K. Hinzer, and M. Baudrit, “Spectrally-resolved measurement of concentrated light distributions for Fresnel lens concentrators,” Opt. Express **24**, 397-407 (2016).

[15] J. Haysom, P. McVey White, L. de la Salle, K. Hinzer, and H. Schriemer, “Multi-year ground-based irradiance dataset in a northern urban climate,” IEEE 43rd Photovoltaic Specialist Conference, Portland, Oregon (2016).

[16] SolarAnywhere® is a database of solar irradiance and associated data, ©2008-2010 by Clean Power Research; https://solaranywhere.com/Public/About.aspx

[17] M. Yandt, K. Hinzer, H. Schriemer, “Efficient multi-junction solar design for maximum annual energy yield by representative spectrum selection,” IEEE J. Photovolt. Manuscript ID: JPV-2016-05-0275-R.R1 (2016)

[18] O. Korech, B. Hirsch, E. A. Katz, and J. M. Gordon, “High-flux characterization of ultrasmall multijunction solar cells,” Appl. Phys. Lett. **91** (2007)

Chapter 6

Conclusion

The progression in the concentrator photovoltaic technology shows its potential as a solution in the continuous search for affordable and effective renewable energy sources. The appeal of CPV is the amount of cross-discipline research put into its success. First, there are mechanical designs since a module has to be mounted on a dual axis tracker to capture the direct normal solar rays. Additionally, there is a large research component to find new materials and optical designs to optimize the potential of an MJSC within a module. To understand how all theses elements interact, elements of each field are used to develop affortable characterization tools. This thesis addressed this issue through the development of a characterization technique to spectrally image the illumination profile of any CPV system.

In chapter 2 the basis of the solar resource, multi-junction solar cell, and concentrators was described in detail. In particular, the thermalization losses in a multi-junction solar cell are reduced when compared to a traditional Si solar cell by 16% since the individual materials absorb a smaller band reducing the thermalization losses. It was established that there have been three distinct generations of Fresnel-based refractive optical architectures. Each generation showed improvement with new development tools exploited. However, due to the temperature dependence and dispersion properties of the materials, refractive optics introduce temperature-influenced illumination patterns that can reduce the absolute efficiency by 3%.

Chapter 3 was a journal publication that discussed in detail the only characterization technique seen to date in the literature that can be used to test any CPV optics and multi-junction solar cell combination. The previous attempts lack this versatility but when multiple bandpass filters are combined with a camera, the spatial and spectral profile can be imaged to within 3% of the actual system electrical output of the individual layers in a multi-junction solar cell, regardless of band gap combination. This experimental set up was the foundation of the ensuing chapters.

All three generations of commercialized CPV systems use refractive optics, which are susceptible to temperature. Chapter 4 is a detailed study of the influence of lens temperature on the full and subcell irradiance profiles of the three different systems. There are two outcomes: First, the refractive index is decreased by a rise in temperature changing the focal distance of the primary. Second, there is a change in the Fresnel structure caused by thermal expansion that broadens the spot illumination beam. In summary, the third generation, 4 Fresnel-Köhler, showed the highest stability since its architecture uses a superposition principle where there are four independent channels, each fully illuminating the multi-junction solar cell. The results show a negligible variation in the optical output over a temperature range of 25 to 55°C, whereas the previous two generations showed a temperature dependence on both the irradiance and subcell profiles. There has been little research on the influence of temperature and this article demonstrates the importance it has on the optical performance of CPV systems.

In chapter 5, the influence of the cell to primary distance, module angular misalignment, and lens temperature of the three CPV generations was discussed. Under non-optimized cell to primary distance, the uniformity of the three generations decrease by a maximum of 15, 10, and 2%, respectively. The effects of the acceptance angle and lens temperature are in the same order of magnitude for each system demonstrating a clear advancement in the newer generations ability to mitigate the effects of different operating conditions on its optical performance. In studying the effects of lens temperature on the energy yield calculations, there was a difference of 9.4, 1.7, and 0.5% in the systems output if a single efficiency value was used.

This experimental technique showed clear correlation between the imaged and measured results. However, there are some changes that can be made to a next generation. The spectral images only cover the top and middle subcells. This is suitable for a triple-junction solar cell but the spectral range needs to be increased to study the new designs that have more subcells. Additionally, a larger temperature range of the thermal chamber is needed to properly represent the outdoor conditions for different suitable locations. Nevertheless, it was demonstrated that the optics of different CPV systems can be accurately characterized in a controlled environment where the outcomes are representative of operating conditions seen when deployed. The aforementioned design improvements will enhance the accuracy of the test bench system for future generations of CPV design. Furthermore, in light of the results discovered, the next generation of CPV optics can be improved to reduce the variations introduced by the thermal effects seen in this thesis. Achromatic and athermal lens can be used in design with a secondary to reduce the effects of temperature on performance.

References

[B - 1] National Energy Board, “Canada’ s Energy Future 2016,” tech. rep., 2016.

[B - 2] J. E. Haysom, O. Jafarieh, H. Anis, K. Hinzer, and D. Wright, “Learning curve analysis of concentrated photovoltaic systems,” *Progress in Photovoltaics: Research and Applications*, vol. 23, pp. 1678–1686, 2015.

[B - 3] Morgan Solar, “LET’S TALK ENERGY WITH... JOHN PAUL MORGAN, MORGAN SOLAR,” *Accessed: January 20, 2016 URL: http://energy.techno-science.ca/en/blogs/337.php.*

[B - 4] C. Gueymard, “The sun’s total and spectral irradiance for solar energy applications and solar radiation models,” *Solar Energy*, vol. 76, no. 4, pp. 423–453, 2004.

[B - 5] F. Vignola, Joseph Michalsky, T. Stoffel, and F. Group, *Solar and IR radiation measurements.* Florida: CRC Press, 1st ed., 2012.

[B - 6] I. Reda and A. A. Nrel, “Solar position algorithm for solar radiation applications,” *Solar Energy*, vol. 76, pp. 577–589, 2004.

[B - 7] C. Gueymard and J. A. Ruiz-Arias, “Validation of direct normal irradiance predictions under arid conditions: A review of radiative models and their turbidity-dependent performance,” *Renewable and Sustainable Energy Reviews*, vol. 45, pp. 379–396, 2015.

[B - 8] C. Gueymard, “Parameterized transmittance model for direct beam and circumsolar spectral irradiance,” *Solar Energy*, vol. 71, no. 5, pp. 325–346, 2001.

[B - 9] P. Ineichen, “Dynamic global-to-direct irradiance conversion models,” *ASHRAE Transactions*, vol. 98, no. 1, pp. 354–369, 1992.

[B - 10] L. Nonnenmacher, A. Kaur, and C. Coimbra, “Verification of the SUNY direct normal irradiance model with ground measurements,” *Solar Energy*, vol. 99, pp. 246–258, 2014.

[B - 11] Z. Sen, *Solar energy fundamentals and modeling techniques.* Springer, 2009.

[B - 12] NREL, “Best Reasearch-Cell Efficiencies,” 2015.

[B - 13] A. Martí and G. Araujo, “Limiting efficiencies for photovoltaic energy conversion in multigap systems,” *Solar Energy Materials & Solar Cells*, vol. 43, pp. 203–222, 1996.

[B - 14] Morgan Solar, “How it works,” *Accessed: January 20, 2016 URL:http://morgansolar.com/how-it-works/.*

[B - 15] M. Buljan, J. Mendes-Lopes, P. Benítez, and J. C. Miñano, “Recent trends in concentrated photovoltaics concentrators’ architecture,” *Journal of Photonics for Energy*, vol. 4, no. 1, p. 040995, 2014.

[B - 16] A. Gombert, J. C. Miñano, P. Benitez, and T. Hornung, “Concentrator Optics for Photovoltaic Systems,” in *Photon Management in Solar Cells* (R. B. Wehrspohn, U. Rau, and A. Gombert, eds.), ch. 6, pp. 153–182, Weinheim, Germany: Wiley-VCH Verlag GmbH & Co. KGaA, 2015.

[B - 17] H. Cotal and R. Sherif, “The effects of chromatic aberration on the performance of GaInP/GaAs/Ge concentrator solar cells from Fresnel optics,” in *31st Photovoltaic Specialists Conference*, (Lake Buena Vista), pp. 747–750, IEEE Xplore, 2005.

[B - 18] P. Sharma, M. Wilkins, H. Schriemer, and K. Hinzer, “Modeling nonuniform irradiance and chromatic aberration effects in a four junction solar cell using SPICE,” in *IEEE 40th Photovoltaic Specialist Conference (PVSC)*, vol. 2, (Denver), pp. 3293–3297, IEEE Xplore, 2014.

[B - 19] Y. Martin, P. D. Kirchner, T. van Kessel, B. Wacaser, R. Sandstrom, D. Patel, B. Kim, A. Badahdah, H. Khonkar, R. Leutz, L. Fu, and H. P. Annen, “High-Concentration Photovoltaics -Effect of Inhomogeneous Spectral Irradiation,” *IEEE Journal of Photovoltaics*, vol. 5, no. 1, pp. 454–460, 2015.

[B - 20] I. García, P. Espinet-González, I. Rey-Stolle, and C. Algora, “Analysis of chromatic aberration effects in triple-junction solar cells using advanced distributed models,” *IEEE Journal of Photovoltaics*, vol. 1, no. 2, pp. 219–224, 2011.

[B - 21] I. García, C. Algora, I. Rey-Stolle, and P. Galiana, “Study of non-uniform light profiles on high concentration III-V solar cells using quasi-3D distributed models,” in *33rd Photovoltaic Specialists Conference (PVSC)*, (San Diego), pp. 1–6, IEEE Xplore, 2008.

[B - 22] H. Baig, K. Heasman, and T. Mallick, “Non-uniform illumination in concentrating solar cells,” *Renewable and Sustainable Energy Reviews*, vol. 16, no. 1, pp. 5890–5909, 2012.

[B - 23] L. James, “Effects of concentrator chromatic aberration on multi-junction cells,” in *IEEE Photovoltaic Specialists Conference (PVSV)*, vol. 2, (Waikoloa), pp. 1799–1802, IEEE Xplore, 1994.

[B - 24] M. Victoria, R. Herrero, C. Domínguez, I. Antón, S. Askins, and G. Sala, “Characterization of the spatial distribution of irradiance and spectrum in concentrating photovoltaic systems and their effect on multi-junction solar cells,” *Progress in Photovoltaics: Research and Applications*, vol. 21, no. 1, pp. 308–318, 2013.

[B - 25] T. Schult, M. Steiner, and P. Nitz, “Temperature dependence of fresnel lenses for concentrating Photovoltaics,” *2nd International Workshop on Concentrating Photovoltaic Optics and Power*, pp. 1–3, 2009.

[B - 26] T. Hornung, A. Bachmaier, P. Nitz, A. Gombert, A. W. Bett, R. D. McConnell, G. Sala, and F. Dimroth, “Temperature Dependent Measurement And Simulation Of Fresnel Lenses For Concentrating Photovoltaics,” *AIP Conference Proceedings*, vol. 85, no. 1277, pp. 85–88, 2010.

[B - 27] V. D. Rumyantsev, N. Y. Davidyuk, E. A. Ionova, P. V. Pokrovskiy, N. A. Sadchikov, and V. M. Andreev, “Thermal Regimes of Fresnel Lenses and Cells in ’All-Glass’ HCPV Modules.,” in *AIP Conference Proceedings*, vol. 1277, pp. 89–92, 2010.

[B - 28] J. E. Haysom, P. McVey White, L. de la Salle, K. Hinzer, and H. Schriemer, “Multi-year Ground-based Irradiance Dataset in a Northern Urban Climate,” in *IEEE 43rd Photovoltaic Specialist Conference (PVSC)*, (Portland), 2016.